Glycosylated extracellular mucin domains protect against SARS-CoV-2 infection at the respiratory surface

Maitrayee Chatterjee[1], Liane Z.X. Huang[1$], Anna Z. Mykytyn[2$], Chunyan Wang[1], Mart M. Lamers[2], Bart Westendorp[3], Richard W. Wubbolts[2], Jos P.M. van Putten[1], Berend-Jan Bosch[1], Bart L. Haagmans[2], and Karin Strijbis[1]*

[1] Department of Biomolecular Health Sciences, Division Infectious Diseases and Immunology, Faculty of Veterinary Medicine, Utrecht University, The Netherlands

[2] Viroscience Department, Erasmus Medical Center, Rotterdam, The Netherlands

[3] Department of Biomolecular Health Sciences, Division Cell Biology, Metabolism and Cancer, Faculty of Veterinary Medicine, Utrecht University, The Netherlands

[$] Equal contribution

* Corresponding author. Email: K.Strijbis@uu.nl

Abstract

Mucins play an essential role in protecting the respiratory tract against microbial infections but can also serve as binding sites for bacterial and viral adhesins. The heavily *O*-glycosylated gel-forming mucins MUC5AC and MUC5B eliminate pathogens by mucociliary clearance while transmembrane mucins MUC1, MUC4, and MUC16 can restrict microbial invasion at the apical surface of the epithelium. In this study, we determined the impact of host mucins and mucin glycans on SARS-CoV-2 epithelial entry. Human lung epithelial Calu-3 cells express the SARS-CoV-2 entry receptor ACE2 and high levels of glycosylated MUC1, but not MUC4 and MUC16, on their cell surface. The *O*-glycan-specific mucinase StcE specifically removed the glycosylated part of the MUC1 extracellular domain while leaving the underlying SEA domain and cytoplasmic tail intact. StcE treatment of Calu-3 cells significantly enhanced infection with SARS-CoV-2 pseudovirus and authentic virus, while removal of sialic acid and fucose from the epithelial surface did not impact viral entry. Both MUC1 and MUC16 are expressed on the surface of human air-liquid interface (ALI) differentiated airway organoids and StcE treatment led to mucin removal and increased levels of SARS-CoV-2 entry and replication. On the surface of Calu-3 cells, the transmembrane mucin MUC1 and ACE2 are often co-expressed and StcE treatment results in enhanced binding of purified spike protein and SARS-CoV-2 pseudovirus. This study points at an important role for glycosylated mucin domains as components of the host defense that can restrict SARS-CoV-2 infection.

Keywords: Mucins, transmembrane mucin, cell-bound mucin, MUC1, MUC16, *O*-linked glycans, sialic acid, fucose, SARS-CoV-2, ACE2, spike, mucin-microbe interactions

Author summary:

SARS-CoV-2, the virus that has caused the devastating COVID-19 pandemic, causes a range of symptoms in infected individuals, from mild respiratory illness to acute respiratory distress syndrome. A fundamental understanding of host factors influencing viral entry is critical to elucidate SARS-CoV-2–host interactions and identify novel therapeutic targets. In this study, we investigated the role of host mucins and mucin glycans on SARS-CoV-2 entry into the airway epithelial cells. Mucins are a family of high molecular weight *O*-glycosylated proteins that play an essential role in protecting the respiratory tract against viral and bacterial infections. The gel-forming mucins MUC5AC and MUC5B clear pathogens by mucociliary clearance while transmembrane mucins MUC1, MUC4, and MUC16 can restrict or facilitate microbial invasion at the apical surface of the epithelium. The mucin-selective protease StcE specifically cleaves the glycosylated extracellular part of the mucins without perturbing

48 the underlying domains. We show that removal of mucins from the surface of Calu-3 cells and primary
49 airway epithelial cultures with StcE mucinase increases binding of the SARS-CoV-2 spike protein to the
50 respiratory surface and greatly enhances infection. This study demonstrates the important role of
51 glycosylated extracellular mucin domains as a host defense mechanism during SARS-CoV-2 entry.
52 Future efforts should be focused on characterizing the role of specific soluble and transmembrane
53 mucins during the different stages of SARS-CoV-2 infection.

54

Introduction

The respiratory mucus system protects the respiratory epithelium against invading pathogens. The major components of mucus are heavily *O*-glycosylated mucin glycoproteins. Soluble mucins are secreted by Goblet cells and provide mucus threads for mucociliary clearance (MCC) of particles and pathogens. Transmembrane mucins are expressed on the apical membrane and cilia and prevent access to epithelial surface receptors. The major mucins of the respiratory system are soluble mucins MUC5AC and MUC5B, and transmembrane (TM) mucins MUC1, MUC4, and MUC16 (1). MUC1 and MUC4 are expressed in the upper and lower airway epithelium, whereas MUC16 expression is restricted to the lower airways (2). The high molecular weight mucin glycoproteins contain domains with extensive *O*-glycan structures that often terminate with charged sialic acids or hydrophobic fucoses that impact their interaction with microbes (3). The expression and glycosylation profiles of mucins are directly influenced by colonization and invasion by bacteria and viruses and are altered during inflammation of the respiratory tract (4). Transmembrane mucins form filamentous structures that extend above the apical surface of the epithelium and these mucins consist of a heavily *O*-glycosylated N-terminal extracellular domain (ED), a single transmembrane domain, and a C-terminal cytoplasmic domain (CT) with signaling capacity. In the lung, MUC1 primarily expresses around microvilli and protrudes at least 100 nm from the cell surface whereas MUC4 (~300 nm in size), and the even larger MUC16 are expressed on the surface of cilia (5). Together, the TM mucins form a barrier that restricts access to the underlying epithelium, act as releasable decoy receptors, and sterically hinders the binding of pathogens to underlying cellular receptors (6). MUC1 has been most extensively studied and implicated in defense against respiratory infections with *Pseudomonas aeruginosa* (7), respiratory syncytial virus (8) and Influenza A virus infection (9). SARS-CoV-2, the coronavirus that is responsible for the COVID-19 pandemic, is an enveloped, single-stranded, positive-sense RNA virus that belong to the β coronavirus genus within the Coronaviridae family (10, 11). SARS-CoV-2 preferentially utilizes angiotensin-converting enzyme 2 (ACE2) as entry receptor by interaction with its envelope-anchored spike protein (12). In addition to ACE2, SARS-CoV-2 entry requires proteolytic cleavage of the spike protein that can be mediated by the transmembrane serine protease 2 (TMPRSS2) (13). Human coronaviruses have also been described to depend on sialic acids linked to glycoproteins or gangliosides as primary attachment sites in the respiratory tract (14). Glycosylated mucins can be decorated with sialic acids and therefore might provide viral binding sites, or on the other hand form a barrier that restricts access to the ACE2 receptor. In this study, we investigated the role of transmembrane mucins and their terminal glycans during SARS-CoV-2 entry in a respiratory cell line and primary airway cultures. We show that MUC1 is abundantly expressed on the respiratory Calu-3 cell line, and that both MUC1 and MUC16 are present on the surface of air-liquid interface (ALI)

differentiated airway organoids. Enzymatic removal of extracellular mucin domains greatly enhances SARS-CoV-2 spike protein binding and viral infection. This study points towards a critical role for transmembrane mucins in limiting SARS-CoV-2 infection.

Results

MUC1 is highly expressed on the surface of ACE2-positive respiratory epithelial cells

The Human Cell Atlas consortium respiratory single cell RNA-seq dataset allows analysis of gene expression in the nasal cavity and proximal, intermediate, and distal respiratory tract (15). We analysed this dataset to determine the expression of ACE2 and mucins in different respiratory cell types present in the nasal (N), and upper and lower respiratory mucosa. ACE2-positive cells included secretory, basal, suprabasal and multiciliated cells. The majority of secretory and multiciliated cells expressed the major TM mucin MUC1 (Fig 1A). Next, we determined the mucin repertoire of ACE2-positive cells in the nasal mucosa and lower respiratory tract. MUC1 was expressed by the majority of cells to a relatively high extent, while TM mucins MUC4 and MUC16 were abundant in multiciliated cells and soluble mucins MUC5AC and MUC5B were highly expressed in secretory and Goblet cells (Fig 1B). This analysis suggests that different respiratory cell types have unique mucin repertoires and that the TM mucin MUC1 is the most abundantly expressed mucin in most types of ACE2-positive respiratory cells.

The human respiratory Calu-3 cell line expresses ACE2 and TMPRSS2 and is highly susceptible to SARS-CoV-2 spike protein-mediated entry (16, 17, 13). We first determined the expression of different mucins and their glycans on Calu-3 cells by immunofluorescence confocal microscopy. Multiple Z-stack images showed expression of MUC1, MUC4, and MUC5AC but only very limited expression of MUC16 (Fig 1C, S1A respectively). To distinguish which mucins are expressed on the extracellular cell surface, we performed immunofluorescence staining without permeabilization of the Calu-3 cells. Using this method, MUC1 was clearly detectable on the cell surface whereas MUC4 and MUC5AC could not be stained indicating intracellular localization (Fig 1D). Next, we determined the expression of the terminal mucin glycans sialic acid and fucose on Calu-3 cells. Immunofluorescence with SNA, MALII, and UEA-I lectin showed the presence of α-2,6 sialic acid, α-2,3 sialic acid, and fucose on Calu-3 cells, respectively (Fig 1F). The α-2,6 sialic acid and α-2,3 sialic acid signals (SNA and MALII) were more prominently detected at the edge of the cell island compared to the fucose signal (UEA1) and some colocalization with MUC1 could be observed. These results demonstrate that Calu-3 cells endogenously express MUC1 on their surface and have abundant expression of sialic acids and fucose.

StcE cleaves the MUC1 glycosylated ED and does not affect ACE2 expression

The StcE mucinase recognizes an *O*-glycosylated serine-threonine motif that is abundant in mucins and is virtually absent in non-mucin proteins (18). We previously applied this bacterial mucinase and its inactive point mutant E447D to remove the MUC1 ED (19). To investigate the effect of StcE on endogenous MUC1 expressed by Calu-3 cells, confocal microscopy was performed on non-treated, StcE-treated and E447D-treated Calu-3 cells and stained with α-MUC1-ED antibody 214D4, α-MUC1-SEA antibody 232A1, and α-MUC1-CT antibody CT2. StcE treatment efficiently removed the glycosylated part of the MUC1 extracellular domain as indicated by a complete loss of α-MUC1-ED 214D4 staining after incubation with the enzyme (Fig 2A). The MUC1 SEA domain and CT are predicted not to be digested by StcE and indeed both domains remained detectable after enzyme treatment (Fig 2B, 2C). We next investigated the effect of StcE, E447D, neuraminidase, and fucosidase treatment on MUC1 by Western blot. Calu-3 cells were incubated with the enzymes for 3 h and then subjected to Western blot analysis with the α-MUC1-ED antibody 214D4 and α-MUC1-CT antibody CT2. After incubation with StcE, the glycosylated part of the extracellular domain of MUC1 (about 450 kDa) was no longer detectable. The high molecular weight MUC1 band was not affected by treatment with the inactive enzyme E447D or fucosidase. After neuraminidase treatment on the other hand, we did observe a reduction of the MUC1 signal compared to the loading control (Fig 2D, E). However, because MUC1 is still detectable on the cellular surface after neuraminidase treatment when using immunofluorescence, we hypothesize that the reduced immunoblot signal could be caused by a change in antibody recognition or altered protein transfer to the nitrocellulose membrane. The observed banding pattern for the MUC1 cytoplasmic tail was not affected by the enzymatic treatments (Fig 2F). Furthermore, we wanted to determine the effect of enzymatic treatment on ACE2 stability because the ACE2 receptor itself is glycosylated (20). No change in expression of the full-length glycosylated ACE2 (nearly 140 kDa) could be observed after treatment with StcE, E447D, neuraminidase, or fucosidase. Interestingly, the soluble form of ACE2 (around 70 kDa) was more prominently detectable after fucosidase treatment (Fig 2G). These results demonstrate that StcE cleaves the glycosylated part of the MUC1 ED without affecting ACE2 expression in Calu-3 cells. To investigate the effect of StcE treatment on *O*-glycosylated surface proteins other than MUC1, we stained the treated and untreated Calu-3 cells with a fluorescently labelled mucin binding domain derived from StcE (X409-GFP) (21). Confocal analysis of non-permeabilized and permeabilized Calu-3 cells demonstrated that there was limited punctate staining with X409 on the Calu-3 surface while MUC1 ED staining showed a more continuous surface staining as previously observed. The MUC1 signal was completely lost after StcE treatment, while some staining remained for X409 (Fig. 2H). With permeabilized cells, a comparable result with a higher level of remaining X409 signal was observed

(Fig. 2I). These results reinforce that MUC1 is highly expressed on the surface of Calu-3 cells, but also demonstrate the presence of some other *O*-glycosylated mucin(-like) proteins.

Enzymatic removal of mucin domains enhances SARS-CoV-2 entry into Calu-3 cells

Next, we investigated whether the sialic acid and fucose residues on glycans or complete glycosylated mucin domain can impact SARS-CoV-2 infection of respiratory cells. Surface α2,3-, α2,6-, and α2,8-linked sialic acids were removed by incubation with neuraminidase and fucose by fucosidase treatment and StcE was used to remove mucin extracellular domains. Neuraminidase treatment for 3 h removed the majority of surface-exposed α2,3- linked sialic acids as detected by MAL-II staining, and α2,6-linked sialic acids detected by SNA staining (Fig S1B). Similarly, fucosidase treatment for 3 h cleaved surface-exposed fucose which was detected by UEA1 staining (Fig S1C). StcE treatment was effective as monitored by removal of the MUC1 glycosylated ED from the cellular surface and reduced X409-GFP staining as describe above (Fig 2,3). After enzymatic treatment of the Calu-3 cells, a SARS-CoV-2 pseudotyped virus carrying the spike protein and encoding a GFP reporter (SARS2-S pseudotyped VSV-GFP) was added in the absence or presence of an anti-spike monoclonal antibody to confirm spike mediated entry of virus and incubated for 24 hours. StcE treatment enhanced the number of SARS2-S pseudotyped VSV-GFP positive cells, while E447D-treated cells did not show enhanced viral entry. No obvious change in viral infection could be observed after neuraminidase or fucosidase treatment (Fig 3A). In all experimental conditions, viral infection was completely blocked in the presence of the monoclonal antibody against the SARS-CoV-2 spike protein demonstrating spike-mediated entry in our experimental setup. The GFP signal was quantified using Image J showing a significant 5.4-fold increase in Calu-3 virus infection after StcE treatment and no significant difference after neuraminidase and fucosidase treatment (Fig 3B).

In an independent set of experiments with a luciferase pseudovirus (SARS2-S pseudotyped VSV-Luc), we also observed a 4-fold increase in viral infection after StcE treatment (Fig 3C). As an additional control, we performed the infection with an VSV-G pseudotyped VSV-Luc that lacks the spike protein. We observed enhanced entry of VSV-G pseudotyped VSV-Luc into Calu-3 after StcE and neuraminidase treatment whereas fucosidase treatment had an opposite effect. As expected, the infection could not be blocked with the anti-SARS2-S mAb (Fig 3D). Confocal microscopy on Calu-3 cells infected with SARS2-S pseudotyped VSV-GFP confirmed that StcE treatment increased the number of infected cells (Fig 3E). Next, we investigated the effect of mucin removal on infection with the authentic SARS-CoV-2 virus. Calu-3 cells were treated with the enzymes and incubated with SARS-CoV-2 virus in the absence or presence of an anti-spike monoclonal antibody for 8 hours to study initial entry. In line with our pseudovirus experiments, we observed a significant increase in the number of infected cells

when cells were treated with StcE mucinase in comparison to control. Again, neuraminidase and fucosidase treatment did not significantly impact viral infection albeit we observed a trend towards increased infection after neuraminidase treatment (Fig 3F). Together these data demonstrate that removal of glycosylated mucin domains results in increased SARS-CoV-2 infection of lung epithelial cells. No effect on viral entry was observed after removing individual glycans sialic acid and fucose.

Negatively charged molecules such as sialic acid or heparan sulphate (HS) on the cellular surface or extracellular matrix proteoglycans have been described to facilitate viral entry (22, 23). Therefore, we investigated if heparanase treatment to remove HS or neuraminidase treatment to remove sialic acids impacted viral invasion after removal of the MUC1 glycosylated domain with StcE. Calu-3 cells were first treated with StcE, followed by treatment with heparanase or neuraminidase and subsequent viral infection with SARS2-S pseudotyped VSV-Luc. Confocal microscopy confirmed the removal of HS and α-2,6 sialic acid from the surface of Calu-3 cells after heparanase and neuraminidase treatment, respectively (Fig S2A, B). Quantification of viral infection showed that the combination treatments did not significantly impact viral invasion compared to StcE only condition (Fig S2C). A small reduction of viral infection was observed when the cells were treated with only heparanase in comparison to the control cells without treatment. All infections in this experiment could be blocked by the mAb demonstrating spike-mediated infection. This result suggests that SARS-CoV-2 entry does not depend on these negatively charged molecules on the cell surface of Calu-3 cells.

StcE treatment of human primary respiratory tissue enhances SARS-CoV-2 infection

To investigate the role of mucins during SARS-CoV-2 infection in epithelial tissue that more closely resembles the human respiratory surface, we performed infection experiments with human ALI-differentiated airway organoids. First, we determined which mucins were expressed in the ALI cultures. Differentiated cultures were prepared for immunofluorescence staining with and without permeabilization and stained with MUC1, MUC4, MUC5AC and MUC16 antibodies. All mucins were detectable in the permeabilized tissues (Fig 4A). In the non-permeabilized tissues transmembrane mucins MUC1 and MUC16 and traces of MUC5AC networks were detectable suggesting that these mucins are expressed on the cellular surface (Fig 4B). Next, we investigated the efficacy of StcE in cleaving MUC1 and MUC16. After StcE treatment, MUC1 staining was still detectable on the surface of the airway organoids (data not shown), but immunoblot analysis of two different donors demonstrated that StcE had effectively cleaved off the glycosylated domain of MUC1 (Fig 4C). The MUC16 antibody recognizes the mucin SEA domain and can therefore not be used to monitor cleavage of the MUC16 glycosylated domain. The X409 domain of StcE was used to detect glycosylated mucin

domains and we found that it colocalized with MUC16, but not with MUC1 (Fig 4D,E). To determine the effect of StcE on surface mucins in general and MUC16 in particular, X409 staining was performed on control ALI cultures and after treatment with StcE and E447D inactive enzyme. A significant reduction of X409 staining could be observed after StcE treatment suggesting cleavage of MUC16 (Fig 4F,G).

To determine the effect of mucin removal on SARS-CoV-2 infection, ALI-differentiated airway organoids from two different donors were treated with StcE, E447D or left untreated followed by infection with authentic SARS-CoV-2 virus. StcE treatment led to a significant increase in SARS-CoV-2 infection and replication in both donors, as measured by RNA copies and infectious virus (Fig 5A-D). Nucleoprotein staining of infected tissues confirmed a high percentage of virus-infected cells in the StcE condition compared to the control and E447D condition (Fig 5E,F).

Removal of mucin domains enhances spike and virus attachment to Calu-3 cells

To understand the spatial relationship between the ACE2 receptor and MUC1, the dominant TM mucin in Calu-3 cells, we performed confocal microscopy on Calu-3 cells stained for ACE2 receptor and the MUC1 extracellular domain with an adjusted protocol that allowed imaging of both proteins. In the monolayer, MUC1- and ACE2-positive cells were observed in distinct scattered distributions (Fig 6A). Some cells expressed both proteins at high levels, while other cells expressed high level of either ACE2 or MUC1. MUC1-negative cells most likely express other mucin-like proteins as demonstrated above (Fig 2H). Next, we investigated if removal of mucin domains directly affected spike and virus attachment to the cellular surface. Calu-3 cells were treated with StcE followed by incubation with purified Fc tagged spike protein (SARS2-S1B-Fc) or SARS2-S pseudotyped VSV-GFP for 1 h at 4°C to monitor attachment and prevent entry. The spike protein was stained without first permeabilizing to prevent intracellular access. In untreated and E447D-treated cells, spike binding was observed in patches along the edge of the cell island while cells treated with StcE showed extensive staining (Fig 6B). Quantification of the fluorescent spike signal on the edges of the cell islands using ImageJ confirmed a significant increase in StcE-treated cells raw spike fluorescence values as determined by integrated density/length (sum of all pixels/µm) (Fig 6C). In a similar experimental setup, we incubated Calu-3 cells with SARS2-S pseudotyped VSV-GFP virus to observe attachment to the cellular surface. In line with the spike-binding assays, we observed more virus attachment to Calu-3 cells after StcE treatment (Fig 6D). In untreated cells, spike-positive pseudoviral particles preferentially bound to areas that stained negative for MUC1 (Fig 4E). Together these results show that enzymatic removal of mucin extracellular domains including the abundant MUC1 ED allows more virus attachment to cells and thus increases infectivity. We propose that the glycosylated domains of transmembrane mucins

such as MUC1 and MUC16 on the respiratory surface form a barrier that prevents SARS-CoV-2 invasion (Fig 6F).

Discussion

The mucosal barrier is the body's first line of defense and offers protection from infection by pathogens. Mucin proteins are known for their barrier properties but can also serve as attachment sites for bacterial and viral pathogens. The findings presented in this study indicate that extracellular mucin domains play a substantial protective role during SARS-CoV-2 infection at the respiratory surface. ACE2-positive cells in the respiratory epithelium express different combinations of mucin genes including MUC1, MUC4, MUC16, MUC5AC and MUC5B of which MUC1 is the most abundantly expressed mucin across different cell types. In this study, we demonstrate that human lung epithelial Calu-3 cells expressed high levels of MUC1, while TM mucins MUC4 and MUC16 and secreted mucin MUC5AC were barely detectable (Fig 1, 2). In airway organoids, MUC1 and MUC16 are expressed on the surface and some secreted MUC5AC is detectable (Fig 4). In different SARS-CoV-2 infection studies with both cell models, we demonstrate that enzymatic removal of extracellular mucin domains, but not individual sialic acid or fucose sugars, enhances viral infection (Fig 3,5). Removal of glycosylated mucin domains from the cellular surface increased binding of purified spike protein and virus to the cellular surface (Fig 6). We propose a model in which glycosylated extracellular mucin domains form a protective layer above the underlying ACE2 receptor thereby preventing access of the virus to the receptor (Fig 6).

There is growing evidence that both soluble and transmembrane mucins play important roles during SARS-CoV-2 infection, but whether their contributions are protective or are facilitating pathogenicity at different stages of disease is still under debate. Mucus hypersecretion and accumulation most likely have a negative impact on disease development due to reduced MCC and mucus plugging (24), but studies into the roles of transmembrane mucins point in different directions. In the course of COVID-19, elevated levels of gel-forming MUC5AC and shed MUC1 can be detected in sputum aspirated from the trachea of patients (25) and high production of MUC5AC was observed in SARS-CoV-2 infected primary respiratory cultures (26). The MUC5B genetic variant rs35705950 is associated with higher expression of the soluble mucin MUC5B and underrepresented in COVID-19 patients compared to healthy individuals, suggesting a protective role for MUC5B (27). In aged individuals, decreased mucus production and weakened MCC might contribute to the higher susceptibility of SARS-CoV-2 (28). Our findings on a protective role for TM mucins MUC1 and MUC16 during SARS-CoV-2 infection are in line

with a recent genome-scale CRISPR loss- and gain-of-function (GOF) study for SARS-CoV-2 entry in human lung epithelial cells overexpressing TM mucins (29). In this GOF study, overexpression of TM mucins MUC1, MUC4 or MUC21 reduced infection by SARS-CoV-2 compared to cells with a non-targeting guide (NTG). The study also demonstrated that enzymatic removal of overexpressed MUC4 resulted in increased viral entry. An important role for MUC4 was also observed during SARS-CoV-1 infection *in vivo* where female MUC4 knockout mice that had enhanced inflammatory cytokine responses and poor prognosis compared to wild type mice (30). Together with our data, these different studies imply that different TM mucins might have a similar protective function during SARS-CoV-2 infection.

In addition to the protective functions of mucins during SARS-CoV-2 initial, there is also emerging evidence that overexpression of different mucins is correlated with severe disease. A MUC1 gene variant that leads to increased expression was one of the few significant loci associated with severe COVID in a large-scale GWAS study. The functional consequences of this gene variation need to be addressed, but the authors suggest that mucins could have a clinically important role in the development of critical illness in COVID-19 (31). This was in line with another study that found increased MUC1 mRNA to be associated with critical disease (32). Single cell sequencing data of COVID-19 patients demonstrated that transmembrane mucins MUC1, MUC4, MUC13 and MUC21 are all highly upregulated in patients with active disease (29) and also in blood samples MUC1 and MUC2 mRNA expression was significantly elevated in critical and mild COVID-19 while MUC16, MUC20 and MUC21 were significantly downregulated in severe COVID (33). Compound R406, the active metabolite of FDA-Approved Fostamatinib that inhibits MUC1 expression is now in clinical trials for hospitalized patients with advanced COVID-19 (34). At this point, we lack the critical insight to conclude if transmembrane mucins in general or MUC1, MUC4 or MUC16 specifically are protective or contributing to disease severity during different stages of pathogenesis within the complexity of the body. It is evident that establishing the function of specific mucins during *in vivo* infection is an important future challenge.

The studies that are currently available underscore the importance of extracellular domain of transmembrane mucins during viral entry. Our confocal microscopy analysis indicates that ACE2-positive cells in the respiratory epithelium often, but not always, express MUC1 and that both proteins colocalize on the apical surface. Enzymatic removal of the MUC1 glycosylated domain did not affect the underlying SEA domain or cytoplasmic tail and ACE2 expression remained detectable. As was previously hypothesized, it is possible that MUC1 and ACE2 interact and/or are in the same protein

complex on the respiratory surface (35). Our data indicate that steric hindrance by glycosylated extracellular mucin domains prevents the virus from reaching the ACE2 receptor (Fig 6). This is in line with a recent study that used mucin mimetics glycopolymers that were capable of shielding surface receptors (36). In a previous study, we have shown that MUC1 ED alters the cell membrane of non-polarized epithelial cells to tubulated morphology and reduce β1-integrin-mediated bacterial invasion (19). In the present study, we have not observed any influence of MUC1 ED on membrane architecture in Calu-3 cells or airway organoids.

Different studies describe that for viral entry SARS-CoV-2 benefits from negatively charged residues like sialic acid-containing glycans or membrane glycosaminoglycans such as heparan sulfate proteoglycans on the cell surface (37, 38, 39). In contrast with this findings, another study reported that neuraminidase treatment of Calu-3 cells only modestly increased SARS-CoV-2 infection (40). In our live virus experiments we did not observe a significant increase in SARS-CoV-2 infection after neuraminidase or fucosidase treatment. We addressed if the negatively charged sialic acids or heparan sulfates were important for viral entry after removal of the glycosylated mucin domain. Consecutive treatment with StcE and neuraminidase or heparinase was performed but did not result in a difference in viral entry (Fig S2). Differences in viral dependence on negatively charged surface molecules maybe be explained by levels of ACE2 and TMPRSS2 protease expression and accessibility of the receptor for the viral spike protein in different cell systems. Therefore, our findings reveal that during infection of human respiratory Calu-3 cells the MUC1 extracellular domain rather than individual mucin glycans prevents the binding of SARS-CoV-2 to the underlying receptor.

Overproduction and excess accumulation of gel-forming mucins in the lungs of COVID-19 patients can lead to airway obstruction and eventually cause life-threatening acute respiratory distress syndrome (41, 42, 43). Several studies are focusing on the reduction of mucin expression overall as a therapeutic strategy (44, 34). In future studies, the role of transmembrane mucins MUC1, MUC4 and MUC16 in disease development should be taken into consideration. A tailored approach that boosts expression of protective transmembrane mucins but reduces secretion of soluble mucins could be an attractive future strategy to prevent infection with SARS-CoV-2 or other respiratory pathogens and improve disease outcome.

Methods

Single cell analysis

Normalized counts and metadata from previously published single cell RNA-sequencing data of healthy human airway epithelium(15) were downloaded from https://www.genomique.eu/cellbrowser/HCA/. Dimensionality reduction was done using the Seurat Package (45) in Rstudio (version 1.2.5019), starting with a principle component analysis. After visual inspection of the principal components using and elbow plot, the first twenty components were used for graph-based clustering analysis. Clusters of cells were then visualized as diffusion maps (uMAPs). To determine gene expression in ACE2- and TMPRSS2-positive versus negative cells we created two additional metadata slots, in which normalized transcript counts of these genes above 0 were considered positive. Then, cell type assignment and normalized expression of a panel of genes of interest was determined by sub-setting single or double-positive epithelial cells.

Cell culture

Calu-3 cells (ATCC Catalog # HTB-55), HEK-293T (ATCC Catalog # CRL-3216) and BHK-21 cells (ATCC Catalog # CCL-10) cells were routinely grown in 25 cm^2 flasks in Dulbecco's modified Eagle's medium (DMEM) containing 10% fetal calf serum (FCS) at 37°C in 5% CO_2.

Human airway organoid culture and differentiation

Adult human lung tissue was obtained from non-tumor lung tissue obtained from patients undergoing lung resection. Lung tissue was obtained from residual, tumor-free, material obtained at lung resection surgery for lung cancer. The Medical Ethical Committee of the Erasmus MC Rotterdam granted permission for this study (METC 2012-512). Human bronchiole and bronchus stem cells were isolated and maintained as described previously (46, 47), using a protocol adapted from Sachs and colleagues (48). Organoids were dissociated using TrypLE express (Gibco) into single cells and plated on Transwell membranes (StemCell) coated with rat tail collagen type I (Fisher Scientific) in Pneumacult-ALI medium (StemCell) and airway organoid medium at a 1:1 ratio as described before (46, 47). Upon confluency, cells were differentiated at an air-liquid interface in 100% Pneumacult-ALI medium for 3-6 weeks. Medium was replaced every 5 days.

Production of SARS-CoV-2 pseudotyped virus and virus neutralization assay

The pseudotyped vesicular stomatitis virus (VSV) was produced by using the protocol of Whitt (49). The detailed protocol of the production of pseudotyped VSV, SARS2-Spike pseudotyped VSV virus and virus neutralization assay is described in the supplementary methods. The optimal working concentration of SARS2-Spike pseudotyped VSV particles (SARS2-S pseudotyped VSV-GFP and SARS2-S pseudotyped VSV-Luc) was determined by viral titration assay on Calu-3 cells.

393

394 **Production of authentic SARS-CoV-2 virus stock**

395 SARS-CoV-2 (isolate BetaCoV/Munich/BavPat1/2020; European Virus Archive Global #026V-03883;
396 kindly provided by Dr. C. Drosten) was propagated on Calu-3 cells in OptiMEM I (1X) + GlutaMAX
397 (Gibco), supplemented with penicillin (100 IU/mL) and streptomycin (100 IU/mL) at 37°C in a
398 humidified CO_2 incubator. Stocks were produced as described previously (50). A detailed description
399 of virus production can be found in the supplementary methods.

400

401 **Enzyme treatment of Calu-3 cells**

402 StcE and StcE-E447D were expressed and purified as described previously (19). For mucinase
403 treatment, Calu-3 cells were treated with 2.5 ug/ml of StcE or its inactive mutant E447D in 10% FCS
404 media for 3 h at 37°C and washed with DPBS. Desialylation of Calu-3 cells was achieved by incubating
405 cells grown in a 96 well plate or 24-well plate or 6 well plate with 100 U/mL α2-3,6,8,9 neuraminidase
406 A (P0722L, NEB) in 10% FCS media for 3 h at 37°C. For fucosidase treatment of Calu-3 cells, 0.4 U/ml
407 of α-(1–2,3,4,6)-L-Fucosidase (E-FUCHS; Megazyme) was added to the cells and incubated for 3 h at
408 37°C. To remove heparan sulfate (HS), 0.1 U/ml heparinase III (H8891-5UN, Sigma) was applied as
409 described for the other enzymes. After enzyme treatment, cells were washed thrice with DPBS and
410 used for subsequent experiments.

411

412 **SARS-CoV-2 infection assays on Calu-3 cells**

413 For infection experiments, Calu-3 cells were grown in 96-well plates and allowed to reach around 90%
414 confluency. Then, cells were treated with enzymes for 3 h at 37°C and 5% CO2, before they were
415 inoculated with SARS2-S pseudotyped VSV-Luc or SARS2-S pseudotyped VSV-GFP. At 20 h post-
416 infection, culture supernatants were aspirated, washed with DPBS, and cells were lysed by overnight
417 incubation with *Renilla* luciferase assay lysis buffer (Promega) at -80°C. The next day, cell lysates were
418 thawed, thoroughly resuspended, and transferred to white, opaque-walled 96-well plates and relative
419 luminescence unit (RLU) was measured. *Renilla* luciferase activity was determined using the Luciferase
420 Assay Systems (Promega) according to the manufacturer's instructions. Raw luminescence values
421 were recorded as counts per 5 seconds by Berthold Centro LB 942 plate luminometer. For SARS2-S
422 pseudotyped VSV-GFP mediated infection, GFP positive signal captured using an EVOS microscope
423 (Thermo Scientific) at 4X magnification and quantified using EVOS software. For infection experiments
424 with the authentic SARS-CoV-2 virus, Calu-3 cells were prepared as described above and inoculated
425 with approximately 200 pfu of SARS-CoV-2. At 8 h post-infection, cells were washed in PBS, fixed in
426 formalin, permeabilized in 70% ethanol and washed in PBS again. Immunofluorescent stainings were

performed as described for SARS-CoV-2 stock production and scanned plates were analyzed using ImageQuant TL software. All work with infectious SARS-CoV-2 was performed in a Class II Biosafety Cabinet under BSL-3 conditions at Erasmus Medical Center.

SARS-CoV-2 infection assays on human airway organoid-derived ALI culture

Prior to infection, ALI cells were washed three times with Advanced DMEM/F12 (Gibco) supplemented with Hepes (20mM, Lonza), Glutamax (Gibco) and Primocin (200ug/ml; Invivogen) (AdDF+++). Cells were pretreated for 3 hours with either 10ug/ml E447D or StcE in AdDF +++ or AdDF +++ alone. Cells were washed three times with AdDF +++ and infected with an MOI of 0.01 of SARS-CoV-2 for 4 hours, at which time cells were washed three times with ADdF +++ and remained on ALI for the duration of the experiment. Apical washes were collected at 4, 24 and 48 hours post infection and viral loads were detected in different treatment conditions. After the last collection cells were fixed in 4% formalin for 20 minutes, followed by 70% ethanol for 20 minutes. Plates were exported from the BSL-3 in ethanol for subsequent staining.

Human airway organoid-derived ALI infection growth curves

All samples were thawed and centrifuged at 2000x g for 5 min to spin down mucus and cellular debris. Supernatant was used for subsequent analysis. Virus titrations to determine pfu/ml were performed as described above for determining SARS-CoV-2 titres. RNA extraction was performed by adding 60 µl of sample to 90 µl MagnaPure LC Lysis buffer (Roche) for 10 minutes. Fifty µl Agencourt AMPure XP beads (Beckman Coulter) were added and incubated for followed by two washes on a DynaMag-96 magnet (Invitrogen) and elution in 30 µl ultrapure water. All steps were performed at room temperature. RNA copies were determined by qRT-PCR using primers targeting the E gene (51) and comparison to a standard curve.

Confocal Microscopy

Cells were grown on coverslips up to 80% confluency were analyzed by immunofluorescent staining. Cells were washed twice with DPBS and fixed with 4% paraformaldehyde in PBS (Affymetrix) for 20 min at room temperature and fixation was stopped with 50 mM NH_4Cl in PBS for 10 min. The staining procedure and antibody details are described in the supplementary methods.

Human airway organoid-derived ALI fluorescent staining

ALI inserts infected with SARS-CoV-2 were fixed in 4% formalin for 20 minutes followed by 70% ethanol for 20 minutes and washed in PBS. Uninfected ALI inserts were either fixed and permeabilized with

0.1% triton-X in 10% normal goat serum (NGS) in PBS or stained live on ice. All inserts were blocked in 10% NGS in PBS for an hour followed by primary antibody incubation overnight or for 4 hours on live cells on ice: rabbit anti-SARS-CoV-2 nucleoprotein (Sinobiological, 40143-T62, 1:1000), mouse anti-MUC1 ED, mouse anti-MUC4, mouse anti-MUC5AC or mouse anti-MUC16 (source and dilution was mentioned in supplementary methods). After incubation with primary antibody, live cells were fixed and washed with PBS. All other inserts were washed with PBS. For secondary antibody incubation, Alexa Fluor 568-conjugated goat α-mouse IgG, Alexa Fluor 488-conjugated goat α-rabbit IgG, Alexa Fluor 647-conjugated goat α-mouse IgG or X409-GFP (source and dilution mentioned in supplementary methods) was used. Secondary antibodies were incubated for one hour. All antibodies were diluted in 10% NGS in PBS. After secondary antibody incubation cells were washed with PBS and stained for nuclei using DAPI diluted in PBS. After 30 minutes incubation cells were washed in PBS and mounted in Prolong Antifade (Invitrogen) mounting medium. ALI culture confocal microscopy was performed on an LSM700 confocal microscope using ZEN software (Zeiss). Representative images are maximum intensity projections taken from Z-stacks. Mean signal intensities of MUC1, MUC16 and X409 were analysed using ZEN software.

Western blotting

Calu-3 cells were grown in 6-well plates for 7 days before enzyme treatment. Enzyme-treated cells were washed thrice with cold DPBS and collected with a scraper. The cell suspension was centrifuged at 5,000 rpm for 5 min at 4°C. Cell pellets were resuspended with 100 µl 1% SDS in presence of a Halt protease inhibitor cocktail and 0.5 M EDTA solution (Thermo Fisher) and cells lysed mechanically by scratching. Protein concentrations were measured using a BCA protein assay kit (23235#, Pierce Company). For detection of the MUC1 ED, 5% mucin gels and a boric acid-Tris system were used as described previously (52). α-MUC1-ED antibody 214D4 was used to detect MUC1 at a dilution of 1:1,000 in TSMT buffer. For detection of the CT of MUC1, 12% SDS-PAGE gel and α-MUC1-CT antibody CT2 was used. For ACE2 detection, 10% SDS-PAGE gel and anti-ACE2 antibody (1:1,000, HPA000288, Sigma-Aldrich) was used. Actin was detected using α-actin antibody (1:5,000; bs-0061R, Bioss). Secondary antibodies used were α-mouse IgG secondary antibody (1:10,000; A2304, Sigma), α-Armenian hamster IgG (1:10,000; GTX25745, Genetex) and α-rabbit IgG (1:10,000; A4914, Sigma). Blots were developed with the Clarity Western ECL kit (Bio-Rad) and imaged in a Gel-Doc system (Bio-Rad).

Statistical Analysis

494 For all experiments, at least three independent biological replicates were performed. Values are
495 expressed as the mean ± SEM of three independent experiments performed in triplicate. Repeated
496 measures one way-ANOVA with Dunnett's or Tukey's or two way-ANOVA with Tukey's post-hoc was
497 applied to test for statistical significance. P values of 0.05 or lower were considered statistically
498 significant. Symbols used are $p > 0.05$ (ns, not significant), $p<0.05$ (*), $p<0.01$ (**), $p<0.001$ (***),
499 $p<0.0001$ (****). The GraphPad Prism 9 software package was used for all statistical analyses.
500
501 **References**

502 **1.** Lillehoj EP, Kato K, Lu W, Kim KC. Cellular and Molecular Biology of Airway Mucins. Int Rev Cell Mol
503 Biol. 2013;303:139-202.
504 **2.** Ridley C, Thornton DJ. Mucins: The frontline defence of the lung. Biochem Soc Trans.
505 2018;46(5):1099–106.
506 **3.** Bennett EP, Mandel U, Clausen H, Gerken TA, Fritz TA, Tabak LA. Control of mucin-type O-
507 glycosylation: A classification of the polypeptide GalNAc-transferase gene family. Glycobiology.
508 2012;22(6):736–56.
509 **4.** Chatterjee M, van Putten JPM, Strijbis K. Defensive properties of mucin glycoproteins during
510 respiratory infections—relevance for sars-cov-2. MBio. 2020;11(6):e02374-20.
511 **5.** Hattrup CL, Gendler SJ. Structure and Function of the Cell Surface (Tethered) Mucins. Annu Rev
512 Physiol. 2008 Mar;70(1):431–57.
513 **6.** Van Putten JPM, Strijbis K. Transmembrane Mucins: Signaling Receptors at the Intersection of
514 Inflammation and Cancer. J Innate Immun. 2017;9(3):281–99.
515 **7.** Ueno K, Koga T, Kato K, Golenbock DT, Gendler SJ, Kai H, et al. MUC1 mucin is a negative regulator
516 of toll-like receptor signaling. Am J Respir Cell Mol Biol. 2008;38(3):263–8.
517 **8.** Li Y, Dinwiddie DL, Harrod KS, Jiang Y, Kim KC. Anti-inflammatory effect of MUC1 during respiratory
518 syncytial virus infection of lung epithelial cells in vitro. Am J Physiol - Lung Cell Mol Physiol.
519 2010;298(4):558–63.
520 **9.** McAuley JL, Corcilius L, Tan HX, Payne RJ, McGuckin MA, Brown LE. The cell surface mucin MUC1
521 limits the severity of influenza A virus infection. Mucosal Immunol. 2017;10(6):1581–93.
522 **10.** da Costa VG, Moreli ML, Saivish MV. The emergence of SARS, MERS and novel SARS-2
523 coronaviruses in the 21st century. Arch Virol. 2020;165(7):1517–26.
524 **11.** Hartenian E, Nandakumar D, Lari A, Ly M, Tucker JM, Glaunsinger BA. The molecular virology of
525 coronaviruses. J Biol Chem. 2020;295(37):12910–34.
526 **12.** Li F. Receptor Recognition Mechanisms of Coronaviruses: a Decade of Structural Studies. J Virol.
527 2015;89(4):1954–64.

528 **13.** Hoffmann M, Kleine-Weber H, Schroeder S, Krüger N, Herrler T, Erichsen S, et al. SARS-CoV-2 Cell
529 Entry Depends on ACE2 and TMPRSS2 and Is Blocked by a Clinically Proven Protease Inhibitor.
530 Cell. 2020;181(2):271–80.
531 **14.** Fantini J, Di Scala C, Chahinian H, Yahi N. Structural and molecular modelling studies reveal a new
532 mechanism of action of chloroquine and hydroxychloroquine against SARS-CoV-2 infection. Int J
533 Antimicrob Agents. 2020;55(5):105960.
534 **15.** Deprez M, Zaragosi L-E, Truchi M, Garcia SR, Arguel M-J, Lebrigand K, et al. A single-cell atlas of
535 the human healthy airways. Am J Respir Crit Care Med. 2020;202**:**1636-1645.
536 **16.** Ou X, Liu Y, Lei X, Li P, Mi D, Ren L, et al. Characterization of spike glycoprotein of SARS-CoV-2 on
537 virus entry and its immune cross-reactivity with SARS-CoV. Nat Commun. 2020;11(1620).
538 **17.** Cagno V. SARS-CoV-2 cellular tropism. The Lancet Microbe. 2020;1(1):e2–3.
539 **18.** Shon DJ, Malaker SA, Pedram K, Yang E, Krishnan V, Dorigo O, et al. An enzymatic toolkit for
540 selective proteolysis, detection, and visualization of mucin-domain glycoproteins. Proc Natl Acad
541 Sci U S A. 2020;117(35):21299–307.
542 **19.** Li X, Wubbolts RW, Bleumink-Pluym NMC, van Putten JPM, Strijbis K. The transmembrane mucin
543 muc1 facilitates b1-integrin-mediated bacterial invasion. MBio. 2021;12(2).
544 **20.** Allen JD, Watanabe Y, Chawla H, Newby ML, Crispin M. Subtle Influence of ACE2 Glycan Processing
545 on SARS-CoV-2 Recognition. J Mol Biol. 2021;433(4):166762.
546 **21.** Nason R, Büll C, Konstantinidi A, Sun L, Ye Z, Halim A, et al. Display of the human mucinome with
547 defined O-glycans by gene engineered cells. Nat Commun. 2021;12(1):1–16.
548 **22.** Milewska A, Zarebski M, Nowak P, Stozek K, Potempa J, Pyrc K. Human Coronavirus NL63 Utilizes
549 Heparan Sulfate Proteoglycans for Attachment to Target Cells. J Virol. 2014;88(22):13221–30.
550 **23.** Lindahl U, Li J ping. Interactions between heparan sulfate and proteins-design and functional
551 implications. Int Rev Cell Mol Biol. 2009;276:105-59.
552 **24.** Kumar SS, Binu A, Devan AR, Nath LR. Mucus targeting as a plausible approach to improve lung
553 function in COVID-19 patients. Med Hypotheses. 2021;156:110680.
554 **25.** Lu W, Liu X, Wang T, Liu F, Zhu A, Lin Y, et al. Elevated MUC1 and MUC5AC mucin protein levels in
555 airway mucus of critical ill COVID-19 patients. J Med Virol. 2021;93(2):582–4.
556 **26.** Morrison CB, Edwards CE, Shaffer KM, Araba KC, Wykoff JA, Williams DR, et al. SARS-CoV-2
557 infection of airway cells causes intense viral and cell shedding, two spreading mechanisms
558 affected by IL-13. Proc Natl Acad Sci U S A. 2022;119(16):1–12.
559 **27.** van Moorsel C, van der Vis J, Benschop C, Ruven H, Quanjel M, Grutters J. The Muc5B Promotor
560 Polymorphism Associates With Severe Covid-19. preprint at
561 https://doi.org/10.1101/2020.05.12.20099333 (2021).

562 **28.** Ho JC, Chan KN, Hu WH, Lam WK, Zheng L, Tipoe GL, et al. The effect of aging on nasal mucociliary
563 clearance, beat frequency, and ultrastructure of respiratory cilia. Am J Respir Crit Care Med.
564 2001;163(4):983–8.
565 **29.** Biering SB, Sarnik SA, Wang E, Zengel JR, Sathyan V, Nguyenla X, et al. Genome-wide, bidirectional
566 CRISPR screens identify mucins as critical host factors modulating SARS-CoV-2 infection. Nat
567 Genet. 2022; 54: 1078–1089.
568 **30.** Plante J, Plante K, Gralinski L, Beall A, Ferris M, Bottomly D, et al. Mucin 4 Protects Female Mice
569 from Coronavirus Pathogenesis. preprint at https://doi.org/10.1101/2020.02.19.957118 (2020)
570 **31.** Kousathanas A, Pairo-Castineira E, Rawlik K, Stuckey A, Odhams CA, Walker S, et al. Whole-genome
571 sequencing reveals host factors underlying critical COVID-19. Nature. 2022;607.
572 **32.** D'alessandro A, Thomas T, Akpan IJ, Reisz JA, Cendali FI, Gamboni F, et al. Biological and clinical
573 factors contributing to the metabolic heterogeneity of hospitalized patients with and without
574 covid-19. Cells. 2021;10(9):1–23.
575 **33.** Smet A, Breugelmans T, Michiels J, Lamote K, Arras W, de Man JG, et al. A dynamic mucin mRNA
576 signature associates with COVID-19 disease presentation and severity. JCI Insight. 2021;6(19):1–
577 20.
578 **34.** Tabassum N, Zhang H, Stebbing J. Repurposing Fostamatinib to Combat SARS-CoV-2-Induced Acute
579 Lung Injury. Cell Reports Med. 2020;1(8):100145.
580 **35.** Bose M, Mitra B, Mukherjee P. Mucin signature as a potential tool to predict susceptibility to
581 COVID-19. Physiol Rep. 2021;9(1):1–10.
582 **36.** Honigfort DJ, Altman MO, Gagneux P, Godula K. Glycocalyx crowding with mucin mimetics
583 strengthens binding of soluble and virus-associated lectins to host cell glycan receptors. Proc Natl
584 Acad Sci. 2021;118(40):e2107896118.
585 **37.** Sun XL. The role of cell surface sialic acids for SARS-CoV-2 infection. Glycobiology.
586 2021;31(10):1245–53.
587 **38.** Clausen TM, Sandoval DR, Spliid CB, Pihl J, Perrett HR, Painter CD, et al. SARS-CoV-2 Infection
588 Depends on Cellular Heparan Sulfate and ACE2. Cell. 2020;183(4):1043–57.
589 **39.** Bò L, Miotto M, Di Rienzo L, Milanetti E, Ruocco G. Exploring the Association Between Sialic Acid
590 and SARS-CoV-2 Spike Protein Through a Molecular Dynamics-Based Approach. Front Med
591 Technol. 2021;2:1–10.
592 **40.** Chu H, Hu B, Huang X, Chai Y, Zhou D, Wang Y, et al. Host and viral determinants for efficient SARS-
593 CoV-2 infection of the human lung. Nat Commun. 2021;12(1):1–15.
594 **41.** He J, Cai S, Feng H, Cai B, Lin L, Mai Y, et al. Single-cell analysis reveals bronchoalveolar epithelial
595 dysfunction in COVID-19 patients. Protein Cell. 2020;11(9):680–7.

596 **42.** Nakashima T, Yokoyama A, Ohnishi H, Hamada H, Ishikawa N, Haruta Y, et al. Circulating KL-
597 6/MUC1 as an independent predictor for disseminated intravascular coagulation in acute
598 respiratory distress syndrome. J Intern Med. 2008;263(4):432–9.
599 **43.** Vestbo J. Epidemiological studies in mucus hypersecretion. Novartis Found Symp. 2002;248:3–12.
600 **44.** Guan WJ, Chen RC, Zhong NS. Strategies for the prevention and management of coronavirus
601 disease 2019. Eur Respir J. 2020 Apr 16;55(4):2000597.
602 **45.** Butler A, Hoffman P, Smibert P, Papalexi E, Satija R. Integrating single-cell transcriptomic data
603 across different conditions, technologies, and species. Nat Biotechnol. 2018;36(5):411–20.
604 **46.** Lamers MM, Beumer J, Vaart J Van Der, Knoops K, Puschhof J, Breugem TI, et al. SARS-CoV-2
605 productively infects human gut enterocytes. Science. 2020;369(6499):50–4.
606 **47.** Lamers MM, Vaart J, Knoops K, Riesebosch S, Breugem TI, Mykytyn AZ, et al. An organoid-derived
607 bronchioalveolar model for SARS-CoV-2 infection of human alveolar type II-like cells. EMBO J.
608 2021;40(5):1–19.
609 **48.** Sachs N, Papaspyropoulos A, Zomer-van Ommen DD, Heo I, Böttinger L, Klay D, et al. Long-term
610 expanding human airway organoids for disease modeling. EMBO J. 2019;38(4):1–20.
611 **49.** Whitt MA. Generation of VSV pseudotypes using recombinant ΔG-VSV for studies on virus entry,
612 identification of entry inhibitors, and immune responses to vaccines. J Virol Methods.
613 2010;169(2):365–74.
614 **50.** Lamers MM, Mykytyn AZ, Breugem TI, Wang Y, Wu DC, Riesebosch S, et al. Human airway cells
615 prevent sars-cov-2 multibasic cleavage site cell culture adaptation. Elife. 2021;10:1–22.
616 **51**. Corman VM, Landt O, Kaiser M, Molenkamp R, Meijer A, Daniel KWC, et al. Detection of 2019 novel
617 coronavirus (2019-nCoV) by real-time RT-PCR. Euro Surveill. 2020;25(3):pii=2000045.
618 **52.** Li X, Bleumink-Pluym NMC, Luijkx YMCA, Wubbolts RW, van Putten JPM, Strijbis K. MUC1 is a
619 receptor for the Salmonella SiiE adhesin that enables apical invasion into enterocytes. PLoS
620 Pathog. 2019;15(2):1–20.
621 **53.** Widjaja I, Wang C, van Haperen R, Gutiérrez-Álvarez J, van Dieren B, Okba NMA et al. Towards a
622 solution to MERS: protective human monoclonal antibodies targeting different domains and
623 functions of the MERS-coronavirus spike glycoprotein. *Emerg. Microbes Infect.* 8, 516–530 (2019).
624 **54.** Schindelin J, Arganda-Carreras I, Frise E, Kaynig V, Longair M, Pietzsch T et al. Fiji: an open-source
625 platform for biological-image analysis. Nat Methods. 2012 Jun 28;9(7):676-82.

626

627 **Acknowledgements**

628 We thank Wentao Li and Arno van Vliet for assistance with virus production. We thank Robert P. de
629 Vries (Faculty of Pharmaceutical Sciences, Utrecht University) for providing expert advice and reagents

for the heparan sulfate experiments. We thank Robbert Rottier for providing human adult lung material. The X409-GFP reagent was kindly provided by Yoshiki Narimatsu (Copenhagen Center for Glycomics). We thank Daphne Stapels for valuable input. MC is supported by One Health funding provided by the Faculty of Veterinary Medicine. KS and LZXH are supported by the European Research Council under the European Union's Horizon 2020 research and innovation program (ERC-2019-STG-852452).

Author Contributions

MC and LZXH performed all Calu-3 characterization and pseudovirus infection experiments. AZM and MML cultured the airway organoids and performed and analyzed the authentic SARS-CoV-2 experiments under supervision of BLH. CW and BJB provided materials and assisted with generation of pseudotyped SARS-CoV-2. BW performed analysis of single cell RNA-seq data. RWW assisted with confocal microscopy. JPMP reviewed the manuscript. KS supervised and helped design all aspects of the study. MC and KS analyzed the results, created the figures, and wrote the manuscript. All authors reviewed the final version of the manuscript.

Competing Interests

We declare no conflict of interest.

Materials and Correspondence

Contact Karin Strijbis (K.Strijbis@uu.nl) for requests and correspondence.

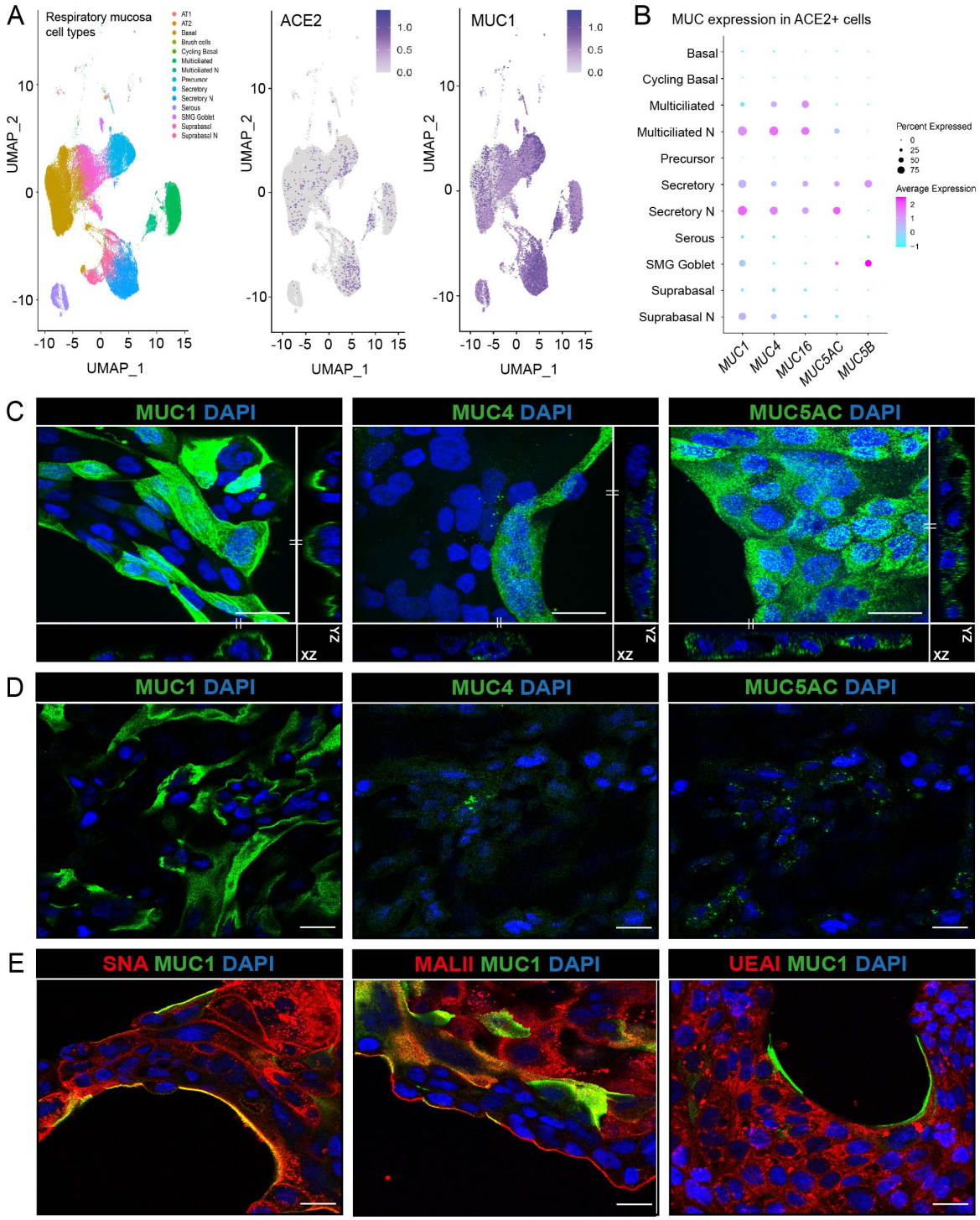

Figure 1. Expression of mucins in respiratory epithelial cells. (A) scRNA-seq analysis of ACE2 and MUC1 expression in different cell types in the respiratory mucosa. Dataset include samples from nasal cavity, upper, intermediate and lower respiratory tract(15). (B) Expression of TM mucins MUC1, MUC4 and MUC16 and gel-forming mucins MUC5AC and MUC5B in ACE2 positive cells. MUC1 is the most highly expressed mucin in ACE2-positive cells. (C) Immunofluorescence confocal microscopy images showing expression of TM mucins MUC1 (214D4, green), MUC4 (8G7, green) and gel-forming mucin MUC5AC (MUC5AC, green) in permeabilized Calu-3 cells. Maximum projections and side views of Z-stacks are shown. (D) Immunofluorescence confocal microscopy without permeabilization showing expression of MUC1 on the surface of Calu-3 cells. MUC4 and MUC5AC

663 could barely be detected suggesting intracellular localization. (E) Immunofluorescence confocal
664 microscopy imaging for α-2,6 sialic acids (SNA, red), α-2,3 sialic acids (MALII, red) and fucose (UEA1,
665 red) in combination with MUC1 (214D4 antibody, green) demonstrates high levels of sialic acid and
666 fucose in Calu-3 cells. Nuclei were stained with DAPI (blue). White scale bars represent 20 µm
667
668

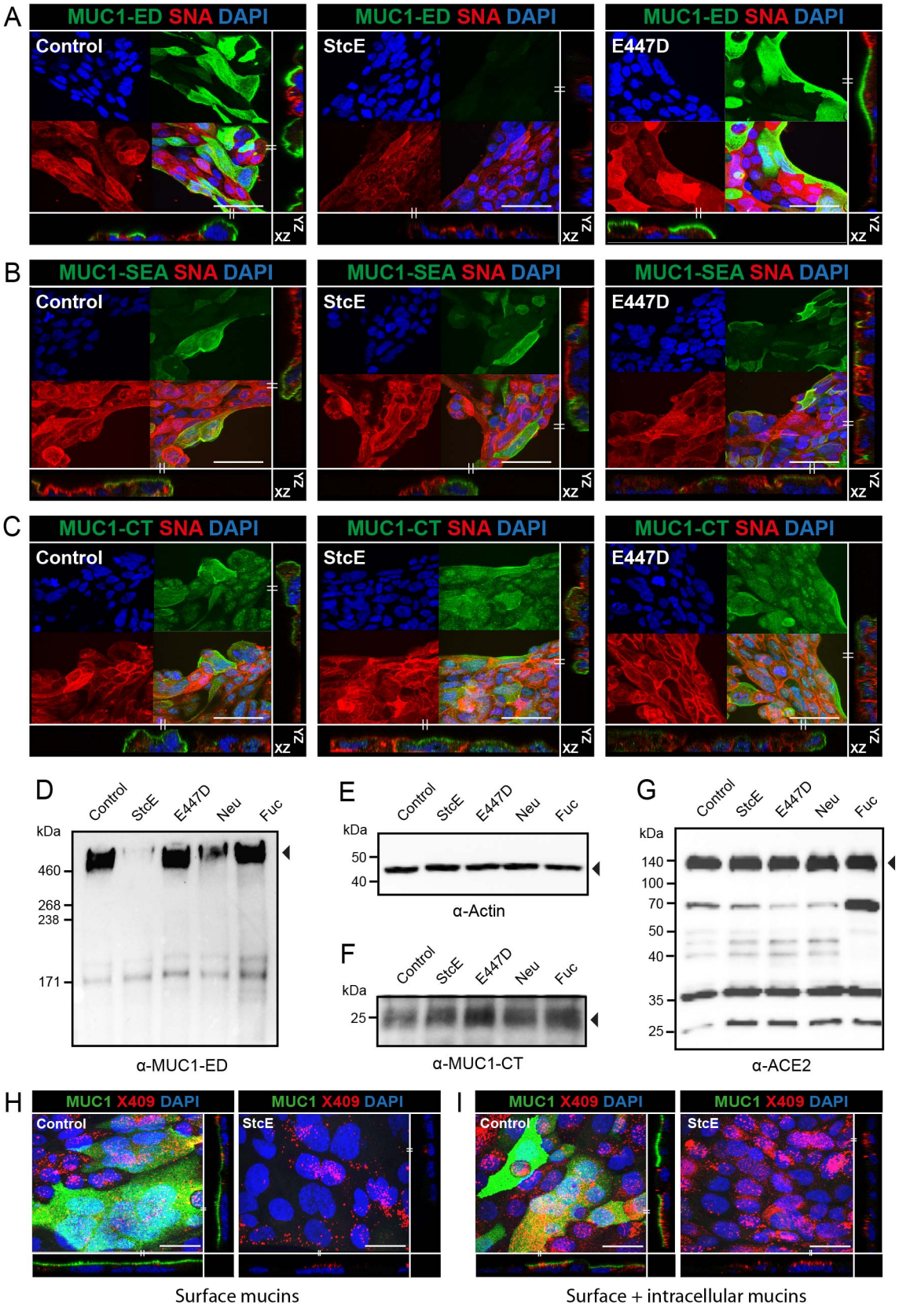

Figure 2. StcE specifically cleaves the glycosylated MUC1 ED and does not affect ACE2 expression. (A) Immunofluorescence confocal microscopy images showing Calu-3 cells treated with StcE or E447D stained for the glycosylated part of the MUC1 extracellular domain (214D4, green) and α-2,6-linked sialic acids (SNA, red). Complete loss of 214D4 signal was observed after treatment with StcE. (B,C)

Immunofluorescence confocal microscopy images of Calu-3 cells as above stained for the MUC1 SEA domain (α-MUC1-SEA antibody 232A1, green) or cytoplasmic tail of MUC1 (α-MUC1-CT antibody CT2, green) in combination with α-2,6-linked sialic acids (SNA, red). The SEA domain and CT were not affected by StcE treatment. Nuclei were stained with DAPI (blue). White scale bars represent 20 µm. Western blot analysis of 7-day grown Calu-3 cells incubated with indicated enzymes for 3 h at 37°C stained with α-MUC1-ED antibody 214D4 (D), β-actin loading control (E), the MUC1 cytoplasmic tail with α-MUC1-CT antibody CT2 (F), and ACE2 (G). StcE treatment removes the MUC1 ED but does not affect the MUC1 CT or ACE2 receptor. (H) Immunofluorescence confocal microscopy images showing Calu-3 cells treated with StcE stained for the glycosylated part of the MUC1 extracellular domain (214D4, green) and fluorescently labelled mucin binding domain derived from StcE (X409-GFP) (X409, red). More continuous surface staining for MUC1 ED and limited punctate staining with X409 on the non-permeabilized cells Calu-3 cells. The MUC1 signal was completely removed after StcE treatment, while some staining remained for X409. (I) Immunofluorescence confocal microscopy images showing, a comparable result with a higher level of remaining X409 signal with permeabilized cells. White scale bars represent 20 µm.

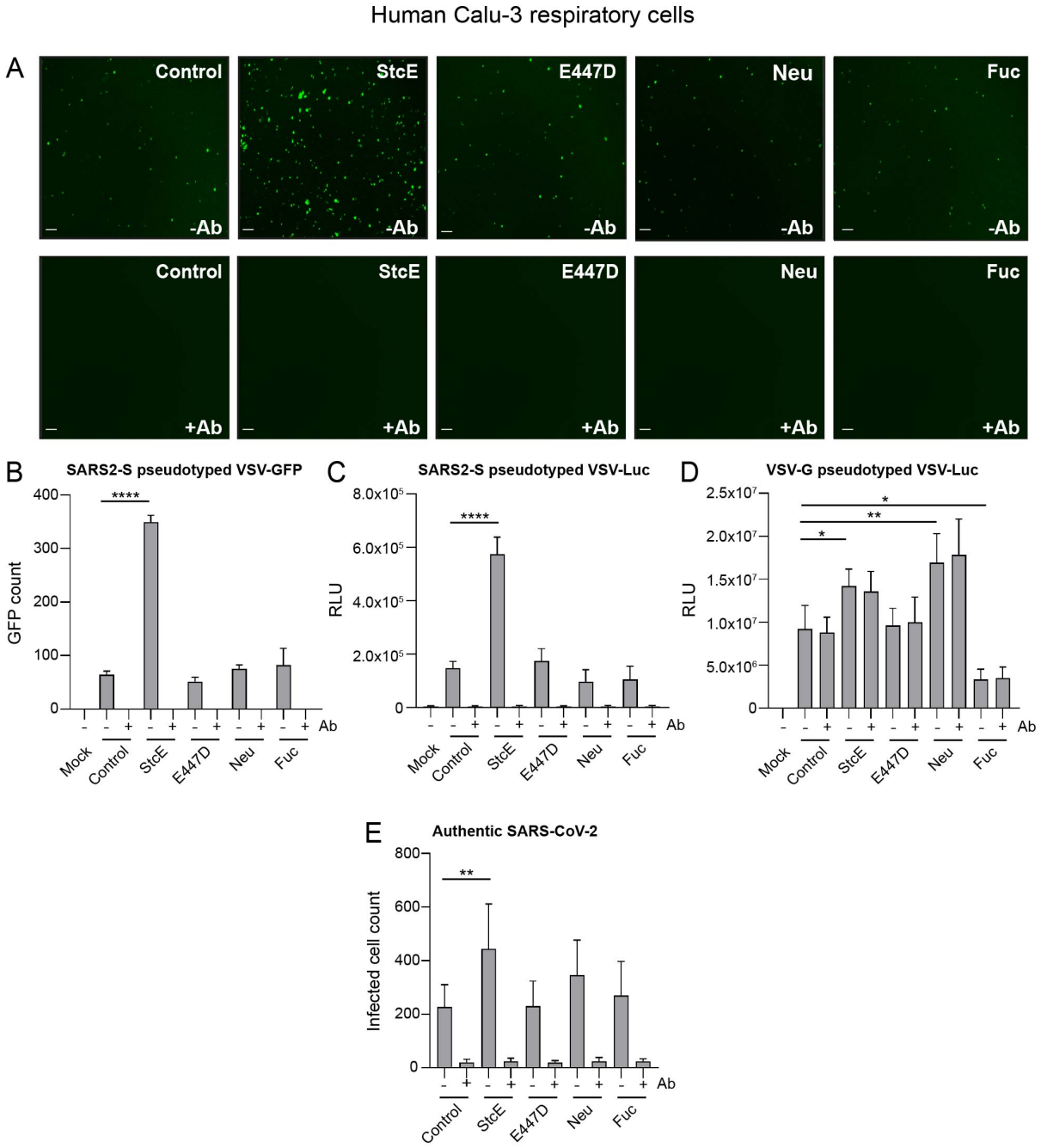

Figure 3. Removal of the glycosylated MUC1 extracellular domain enhances SARS-CoV-2 entry. (A) Microscopy images of Calu-3 cells treated with StcE, E447D, neuraminidase or fucosidase infected with SARS2-S pseudotyped VSV-GFP without or with neutralizing monoclonal antibody (mAb) against SARS2-Spike. White scale bars represent 200 µm. (B) Quantification of SARS2-S pseudotyped VSV-GFP signal in Calu-3 cells using EVOS software. StcE treatment resulted in a 5.4-fold increase in infection. (C) Quantification of luciferase signal (RLU) in Calu-3 cells after treatment with indicated enzymes and infection with SARS2-S pseudotyped VSV-Luc in the absence or presence of mAb against spike. A 4-fold increase in RLU value was observed when cells were treated with StcE. (D) Quantification of Calu-3 cell infection with VSV-G pseudotyped VSV-Luc lacking the spike protein. Infection was not blocked by the anti- spike mAb. (E) Infection of Calu-3 cells with authentic SARS-CoV-2 after treatment with indicated enzymes. StcE treatment resulted in a 2-fold increase in infected cell count. Neuraminidase and fucosidase treatment did not significantly impact viral entry. Represented values are the mean ± SEM of three biological replicates performed in triplicate. Statistical analysis was performed by

repeated measures one way-ANOVA with Dunnett's post-hoc test. $p > 0.05$ [ns, not significant], $p<0.05$ [*], $p<0.01$ [**], $p<0.001$ [***], $p<0.0001$ [****].

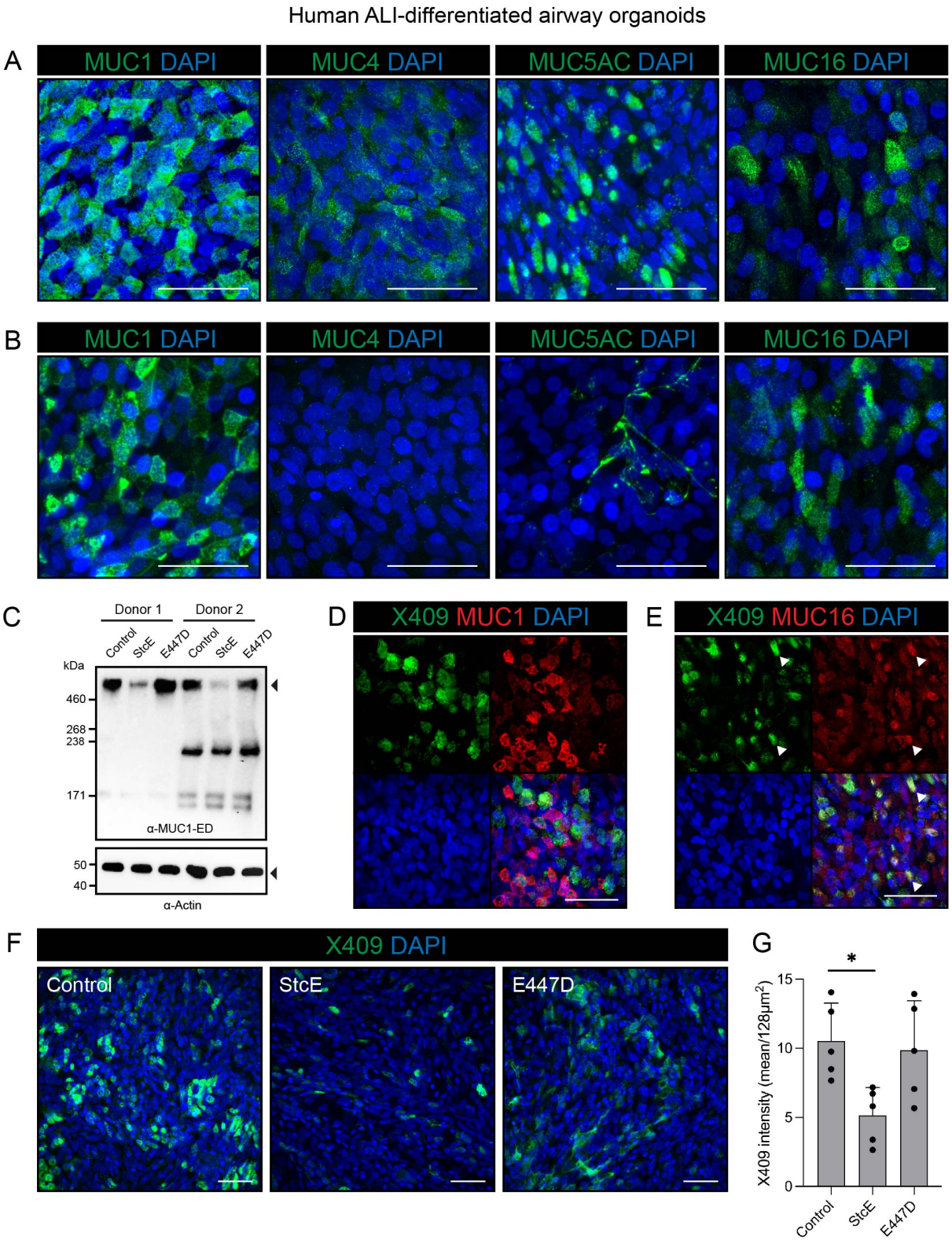

Figure 4. MUC1 and MUC16 are expressed on the surface of human airway organoid-derived air-liquid interface cultures and decreases upon StcE treatment. (A) Microscopy of permeabilized human airway organoid-derived air-liquid interface cultures showing combined extracellular and intracellular staining of MUC1, MUC4, MUC5AC and MUC16. (B) Microscopy of live stained air-liquid culture for MUC1, MUC4, MUC5AC and MUC16 without permeabilization. MUC1 and MUC16 are detectable demonstrating expression on the cell surface, whereas MUC4 staining is negative and MUC5AC only

stains positive in occasional mucus strands on top of the cells. (C) Immunoblot analysis of MUC1 levels in human airway organoid-derived air-liquid interface cultures from donor 1 and donor 2 treated with StcE, E447D or no treatment. The high molecular weight MUC1 is removed upon StcE treatment. (D, E) Microscopy of MUC1 (D) and MUC16 (E) in permeabilized air-liquid cultures along with *O*-glycan probe X409-GFP. Arrows indicate co-localization of X409 with MUC16, but not MUC1. (F) Microscopy of surface binding of X409 on untreated, 10ug/ml StcE and 10ug/ml E447D treated air-liquid cultures. All white scale bars indicate 50 μm. (G) Quantification of X409 signal intensity per imaged field from experiment performed in E. Statistical analysis was performed by repeated measures one way-ANOVA with Tukey's post-hoc test. $p<0.05$ [*].

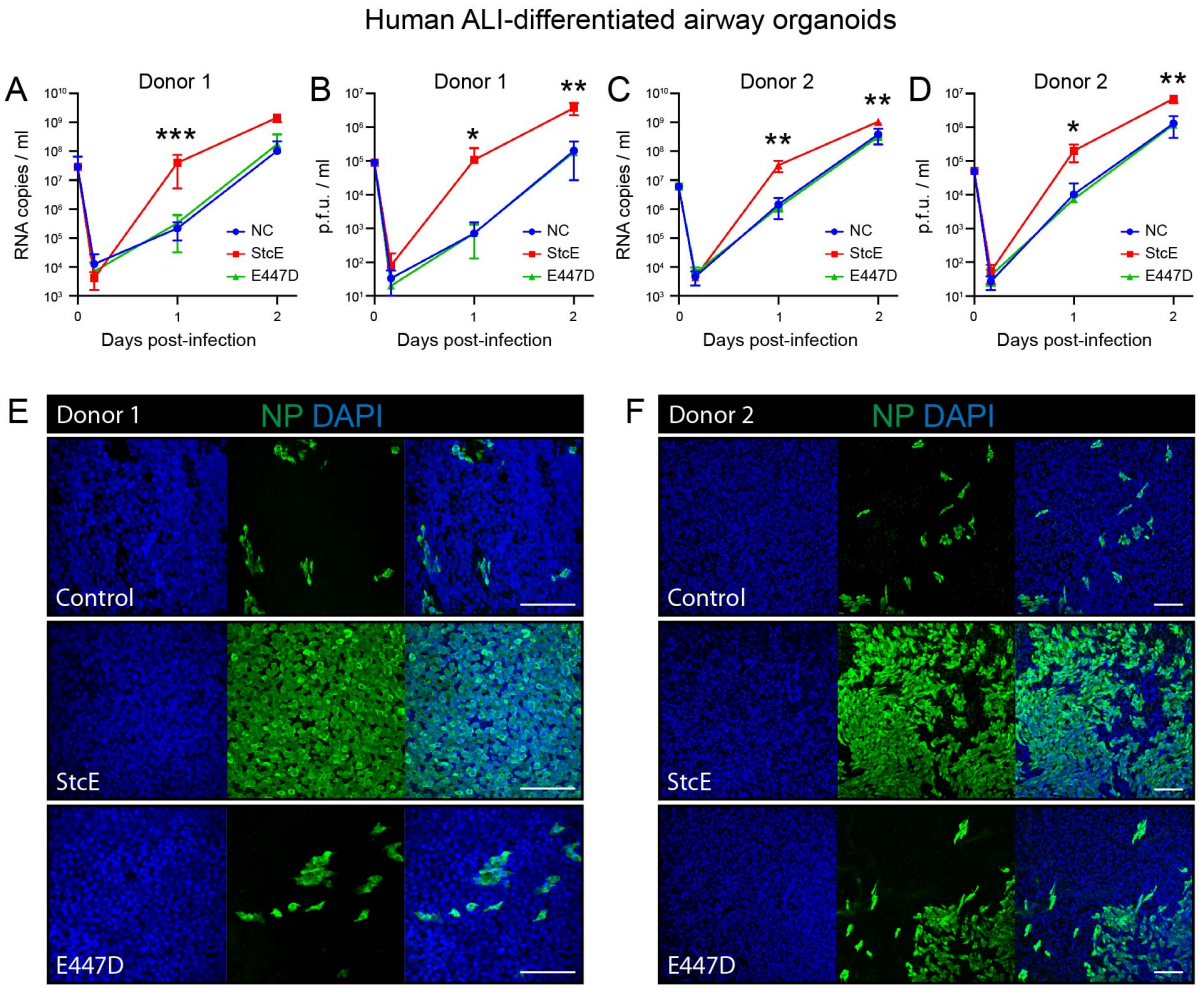

Figure 5. StcE treatment of human airway organoid-derived air-liquid interface cultures increases SARS-CoV-2 replication. (A-D) Replication kinetics of SARS-CoV-2 in air-liquid interface cultures in terms of RNA copies (A, C) and infectious virus (B, D) in two donors. Represented values are the mean ± SD of three replicates. Statistical analysis was performed for donor 2 by repeated measures two way-ANOVA with Tukey's post-hoc test. $p<0.05$ [*], $p<0.01$ [**], $p<0.001$ [***], $p<0.0001$ [****]. $p<0.01$ was found between NC and StcE and E447D and StcE treated cells at 1 day post infection and at 2 days post infection between E447D and StcE treated cells (C). $p<0.05$ was found between NC and StcE and E447D and StcE treated cells at 2 days post infection (D). (E-F) Microscopy images of untreated, 10ug/ml E447D or 10ug/ml StcE treated cells from donor 1 (E) or donor 2 (F), infected with SARS-CoV-2 at two days post-infection. White scale bars represent 100 μm. NP=nucleoprotein.

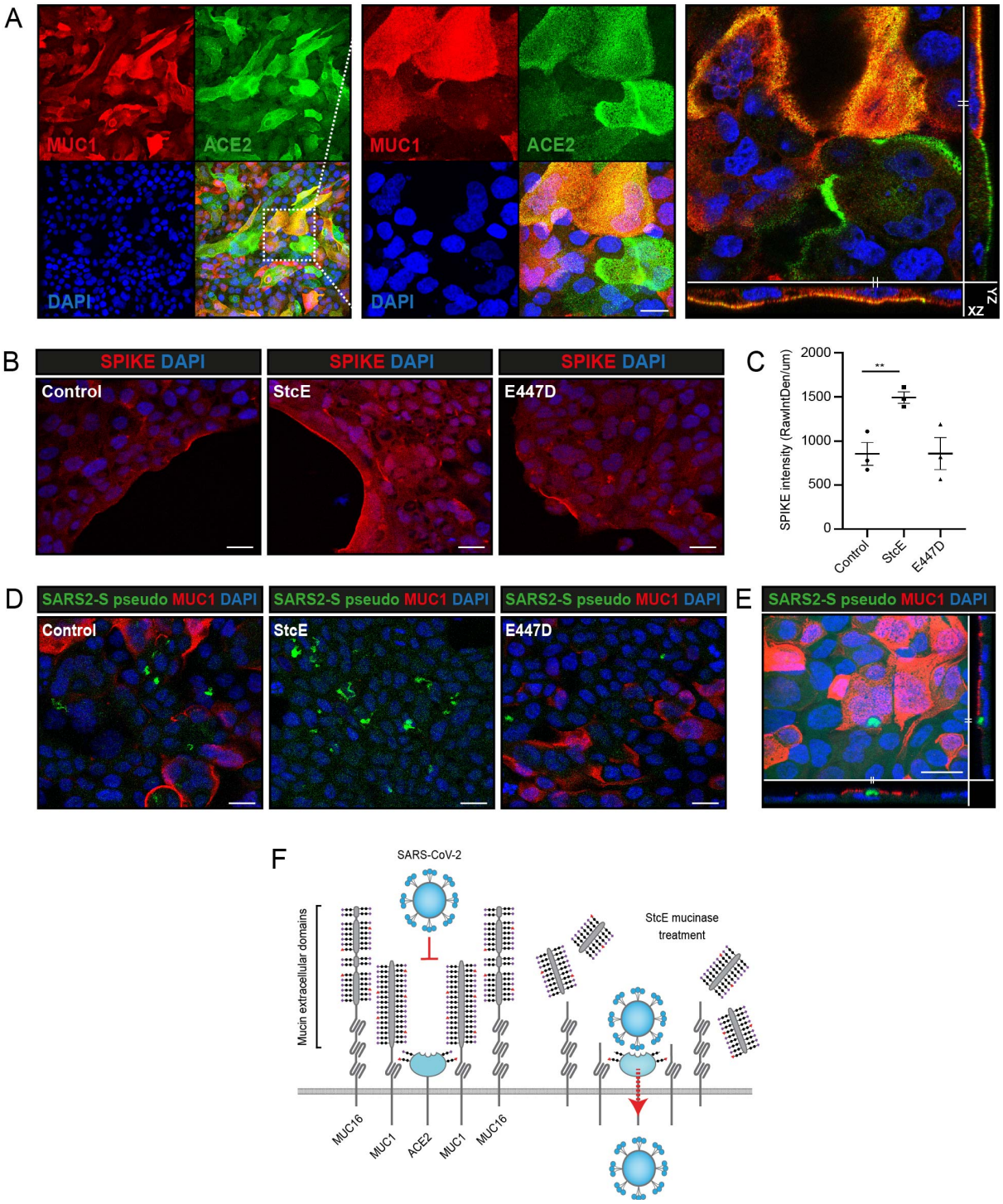

Figure 6. Removal of the MUC1 extracellular domain increases spike and virus attachment.
(A) Immunofluorescence confocal microscopy analysis of expression and localization of ACE2 (green) and TM mucin MUC1 (214D4, red) in Calu-3 cells. (B) Immunofluorescence confocal microscopy of Calu-3 cells incubated with 2.5 ug/ml SARS-CoV-2 spike (Fc-tagged SARS2-S1B-Fc, red) at 4°C for 1 h. Spike was stained without permeabilization. Increased spike binding and higher spike signal intensity was observed after treatment with StcE in comparison to E447D treatment and control. (C) Quantification of spike fluorescence signal as depicted in B. Fluorescence intensity along the edge of cell island was determined in control, StcE- and E447D-treated cells using ImageJ. Mean ± SEM raw integrated density/length from three random fields from three independent experiments are plotted. The area of spike binding was significantly higher in StcE-treated cells. (D) Immunofluorescence

confocal microscopy of Calu-3 cells incubated with SARS2-S pseudotyped VSV-GFP (green) at 4°C for 1 h. Complete disappearance of MUC1 ED signal (214D4, red) and increased virus attachment (green) and was observed in StcE-treated cells. Nuclei were stained with DAPI (blue). (E) Confocal microscopy image showing spike-positive pseudoviral particles preferentially attach to a MUC1-negative surface before invasion. White scale bars represent 20 µm. (F) Working model describing the protective functions of the extracellular domains of transmembrane mucins MUC1 and MUC16 during SARS-CoV-2 infection. The extended glycosylated extracellular domains prevent access of the virus to the ACE2 receptor (left). Enzymatic removal of the glycosylated part of the extracellular domains with the StcE mucinase allows the viral spike protein to connect with the ACE2 receptor resulting in viral entry into lung epithelial cells (right).

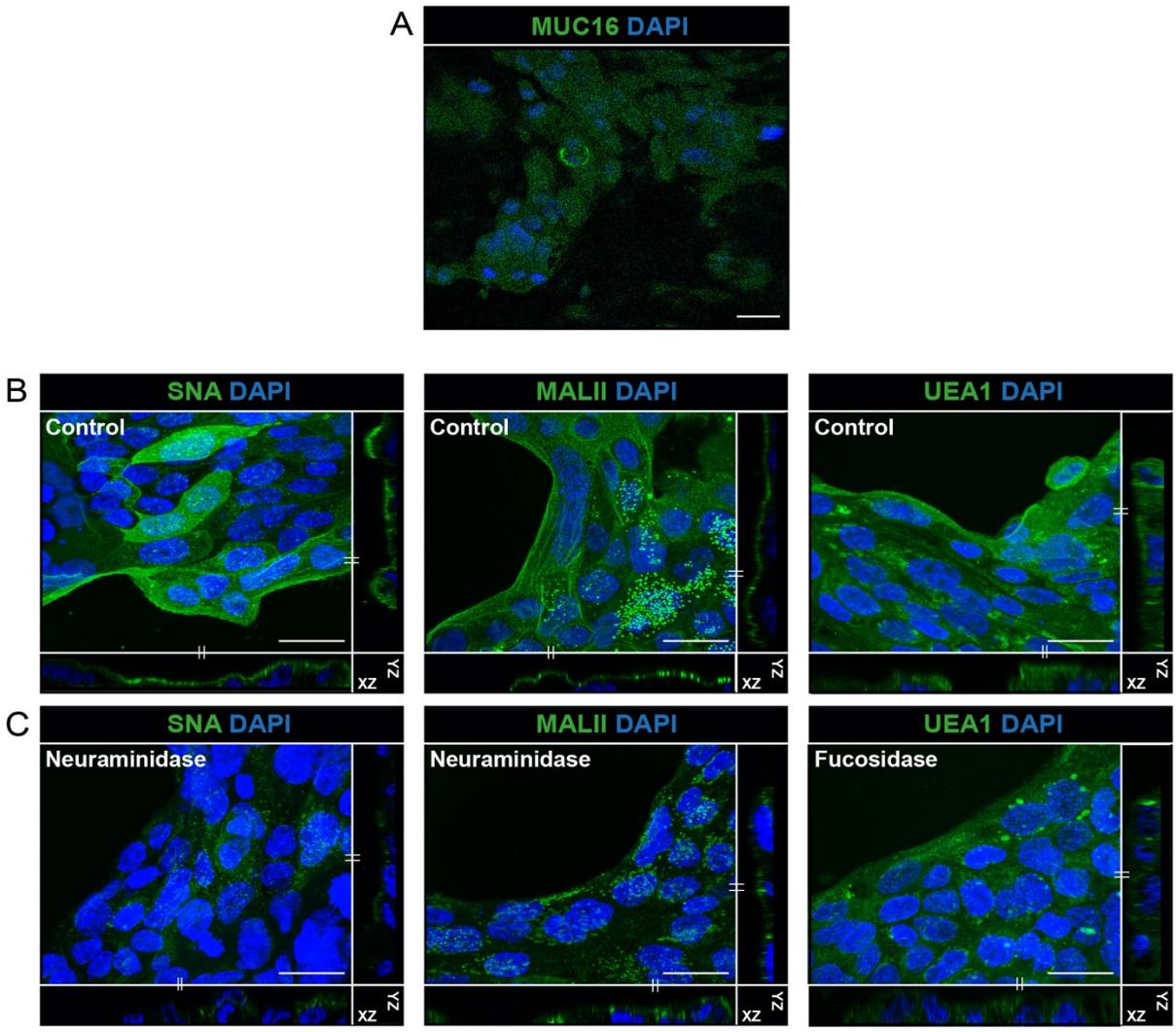

Figure S1. Characterization of expression of mucins and mucin glycans on Calu-3 cells. (A) Immunofluorescence confocal microscopy of 4-days grown Calu-3 cells revealed very limited expression of MUC16 (α-MUC16 ED, green). (B) Immunofluorescence confocal microscopy images for α-2,6 sialic acid (SNA, green) and α-2,3 sialic acid (MALII, green) levels after neuraminidase treatment and fucose (UEA1, green) after fucosidase treatment of Calu-3 cells. Nuclei were stained with DAPI (blue). White scale bars represent 20 µm.

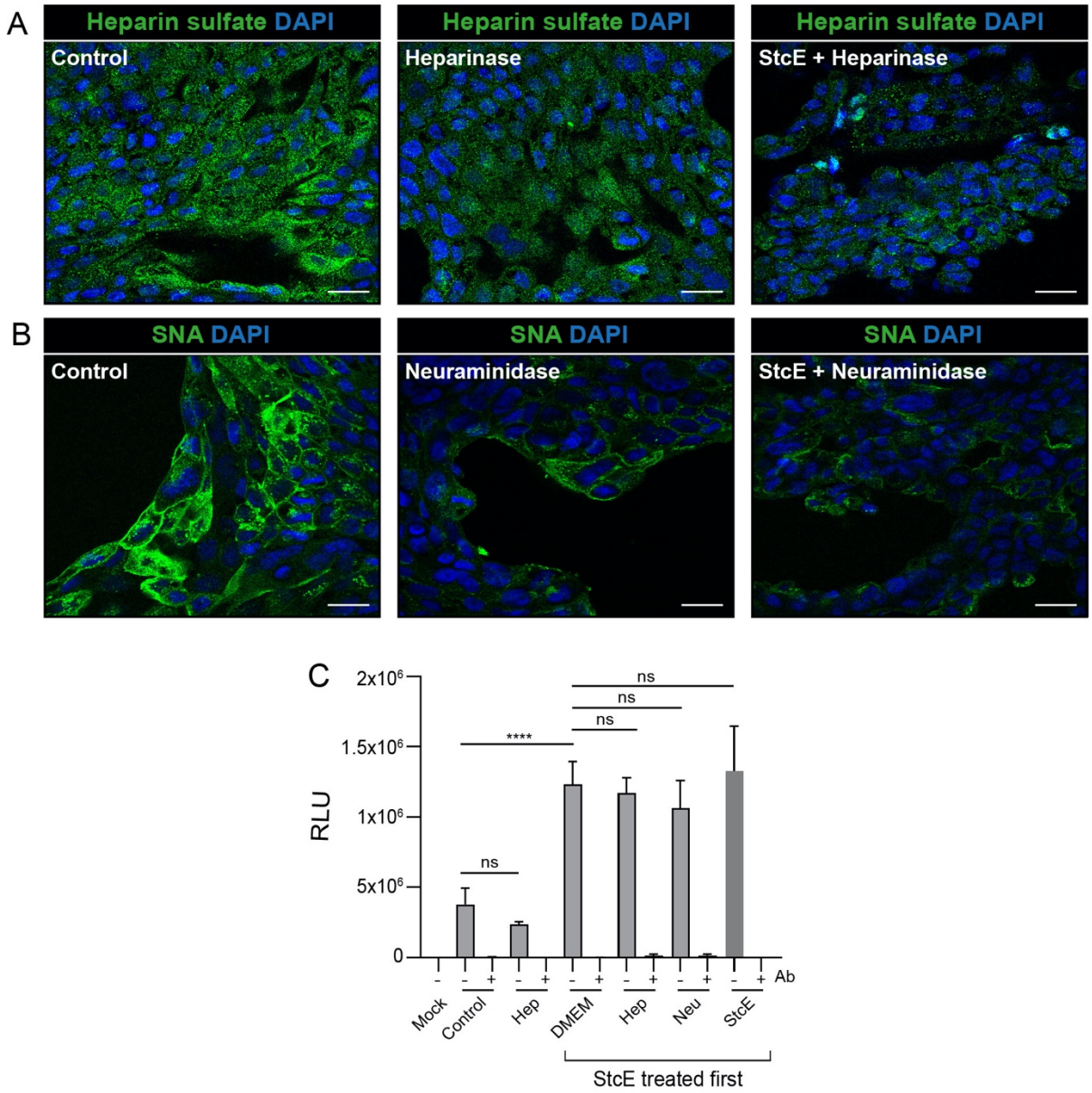

763

764 **Figure S2.** Heparinase or neuraminidase treatment in combination with mucinase does not affect
765 SARS-CoV-2 entry.
766 (A) Confocal microscopy image showing levels of heparin sulfate (F69-3G10, green) in control,
767 heparinase-treated and StcE/heparinase-treated Calu-3 cells. (B) Confocal microscopy image showing
768 levels of α-2,6 sialic acid (SNA, green) control, neuraminidase-treated and StcE/neuraminidase-treated
769 Calu-3 cells. Nuclei were stained with DAPI (blue). White scale bars represent 20 µm. (C) Luciferase
770 quantification of viral infection of Calu-3 cells were treated with StcE for 3 h at 37°C followed by
771 heparinase or neuraminidase for an additional 3 h at 37°C and infection with VSVΔG-Rluc*SARS2-Spike
772 without or with monoclonal antibody (mAb) against SARS2-Spike. No significant changes in RLU values
773 were observed in any of the cases. Represented values are the mean ± SEM of three biological
774 replicates performed in triplicate. Statistical analysis was performed by repeated measures one way-
775 ANOVA with Dunnett's post-hoc test. $p > 0.05$ [ns, not significant], $p<0.05$ [*], $p<0.01$ [**], $p<0.001$
776 [***], $p<0.0001$ [****].

Supplementary methods

Production of pseudotyped vesicular stomatitis virus (VSV) and SARS2-Spike pseudotyped VSV virus

BHK-21 cells were co-transfected with the plasmids pVSVΔG-GFP (green fluorescent protein reporter) or pVSVΔG-Rluc (*Renilla reniformis* luciferase reporter) and the four assembly plasmids encoding the VSV-N, -P, -G and -L proteins. The VSVΔG-GFP and Rluc virus stocks were harvested and added to BHK-21 cells that were transfected with pCAGGS expression vector encoding VSV-G glycoprotein for the production of VSV-G pseudotyped VSV-GFP and VSV-G pseudotyped VSV-Luc virus. After 48 h, supernatant containing VSV-G pseudotyped VSV-GFP or VSV-G pseudotyped VSV-Luc viral particles were harvested and used for the production of SARS2-Spike pseudotyped VSV-GFP or SARS2-Spike pseudotyped VSV-Luc respectively according a previously described method (53).

For the production of SARS-CoV-2 pseudotyped virus, HEK-293T cells were transfected with a pCAGGS expression vector encoding SARS-CoV-2 Spike carrying an 18-a.a. cytoplasmic tail truncation (SARS2-S-d18-Flag). Two days post-transfection, cells were infected with the VSV-G pseudotyped VSV-GFP or VSV-G pseudotyped VSV-Luc at a multiplicity of infection (MOI) of 1. After 4 h of infection, infection medium was removed and washed thoroughly to remove surface-attached VSV pseudovirus. Twenty-four hours later, supernatants containing SARS2-Spike pseudotyped VSV particles (SARS2-S pseudotyped VSV-GFP and SARS2-S pseudotyped VSV-Luc) were harvested and stored at -80°C until use. For the virus neutralization assay, monoclonal antibody (mAb) REGN10933 against SARS2-Spike (developed in the group of Berend Jan Bosch) was used at a final concentration of 1 μg/ml in DMEM supplemented with 1% FCS (Gibco), 100 U/ml Penicillin and 100 μg/ml Streptomycin. Diluted mAbs were incubated with an equal volume of SARS2-S pseudotyped VSV-GFP or SARS2-S pseudotyped VSV-Luc viral particles for 1 hour at room temperature, followed by inoculation on confluent Calu-3 cells in a 96-well plate and incubation at 37°C for 18-20 h. Luciferase activity was measured on a Berthold Centro LB 942 plate luminometer using the *Renilla* luciferase substrate coelenterazine (Promega). The percentage of infectivity was determined as a ratio of luciferase signal in the absence of mAbs normalized to luciferase signal in the presence of mAb.

Production of authentic SARS-CoV-2 virus stock

Briefly, cells were infected at a MOI of 0.01 and incubated for 48-72 h. Collected supernatant was cleared by centrifugation before being additionally cleared using a 0.45 μM low protein binding filter (Millipore) to remove mucus debris produced by the cells. The medium was exchanged three times with Opti-MEM I (1X) + GlutaMAX (Gibco) using an Amicon Ultra-15 column (100 kDa cutoff). After three exchanges, the purified virus was transferred to a new 50 ml tube and the Amicon Ultra-15 column was washed with 1 ml Opti-MEM I (1X) + GlutaMAX (Gibco), adding each wash to the tube

containing the purified virus preparation until the volume in the purified virus stock was equal to the original volume of culture supernatant. Purified virus was stored at −80°C in aliquots. Stock titers were determined by plaque assay. Briefly, 10-fold serial dilutions were performed in 2 ml Opti-MEM I (1X) + GlutaMAX (Gibco). One ml of each virus dilution was added to monolayers of Calu-3 cells in the same medium in a 12 well plate. Cells were incubated at 37°C for 1 hr and then overlaid with 1.2% Avicel (FMC biopolymers) in Opti-MEM I (1X) + GlutaMAX (Gibco) for 72 hours. Next, cells were washed once in PBS, fixed in formalin, permeabilized in 70% ethanol and washed in PBS again. Cells were blocked in 3% BSA (bovine serum albumin; Sigma) in PBS, stained with mouse anti-nucleocapsid (Sino biological; 1:1000) in PBS containing 0.1% BSA, washed three times in PBS, then stained with goat anti-mouse Alexa Fluor 488 (Invitrogen; 1:2000) in PBS containing 0.1% BSA and then washed three times in PBS. All staining steps were performed at room temperature for one hour. Plates were scanned on the Amersham Typhoon Biomolecular Imager (channel Cy2; resolution 10 µm; GE Healthcare). All work with infectious SARS-CoV-2 was performed in a Class II Biosafety Cabinet under BSL-3 conditions at Erasmus Medical Center.

Confocal microscopy

For staining of the α-MUC1 ED, α-MUC1 SEA, α-MUC4 ED, α-MUC16 ED, α-MUC5AC, SNA, MALII, UEA1, ACE2, and Spike, fixed cells on coverslips were permeabilized in binding buffer containing 0.1% saponin (Sigma) and 0.2% BSA (Sigma) in DPBS for 30 min. After permeabilization, cells were washed two times with DPBS and incubated onto 50-µl drops containing 214D4 antibody (CD227, Nordic MUbio) for α-MUC1 ED, 232A1 antibody (a kind gift from Dr. John Hilkens, AVL Amsterdam) for α-MUC1 SEA, α-MUC4 ED (8G7; sc-53945, Santa Cruz Biotechnology), α-MUC5AC (ab198294, Abcam), α-MUC16 ED (a kind gift from Ulla Mandel, University of Copenhagen, Denmark), biotinylated-SNA (B-1305-2; Vector Lab), biotinylated-MALII (B-1265-1; Vector Lab), biotinylated-UEA1 (B-1065-2; Vector Lab), ACE2 (ab272690, Abcam), Heparin sulphate (370260-S; Amsbio) diluted 1:100 and Fc-tagged SARS2-S1B-Fc (a kind gift from Berend Jan Bosch, Utrecht University) diluted 1:164 in the binding buffer on parafilm for 1 h at RT. For staining of the MUC1 CT domain, cells on coverslips were permeabilized in DPBS containing 0.2% Triton X-100 (Merck) for 10 min. After permeabilization, cells were blocked with 1% BSA and 22.5 mg/ml glycine in PBST (DPBS + 0.1% Tween 20 [Sigma]) for 30 min and washed three times with DPBS. Cells were incubated onto 50-µl drops of the α-MUC1-CT antibody (ab80952, Abcam) diluted 1:100 with 1% BSA in PBST on parafilm for 1 h at RT. For non-permeabilization microscopy, the cell permeabilization step was omitted and primary antibody was used in 0.2% BSA in DPBS for 1 h at RT. After removing the primary antibody, 3 washing steps were performed. The coverslips were further incubated with the secondary antibodies Alexa Fluor 488-

conjugated goat α-mouse IgG (1:100; A11029, Thermo Fisher), Alexa Fluor 568-conjugated goat α-mouse IgG (1:100; A11031, Thermo Fisher), Alexa Fluor 647-conjugated goat α-mouse IgG (1:100; ab150115, Abcam), Alexa Fluor 488-conjugated goat α-rabbit IgG (1:100; A11034, Thermo Fisher), Alexa Fluor 488-conjugated goat α-Armenian hamster IgG (1:100, ab173003, Abcam), Alexa Fluor 594-conjugated goat α-human IgG (1:400; A-11014, Thermo Fisher), Streptavidin-488 (1:100; A6374, Thermo Fisher) and 568 (1:100; S11226, Thermo Fisher) and DAPI at 2 µg/ml (D21490, Invitrogen) for 1 h. Coverslips were washed 3 times with DPBS, washed a final time with MilliQ, dried, embedded in Prolong diamond mounting solution (Thermo Fisher), and allowed to solidify overnight at RT. For initial attachment of spike and virus study, 2.5 ug/ml purified Fc-tagged spike protein of SARS-CoV-2 (SARS2-S1B-Fc) and VSVΔG-GFP*SARS2-Spike was added to Calu-3 cells at 4°C for 1 h after StcE and E447D treatment. Cells were washed thoroughly to remove unbound spike/virus before fixation and followed the non-permeabilization protocol for staining. For the 20 h infection study, VSVΔG-GFP*SARS2-Spike was added to Calu-3 cells after StcE and E447D treatment and incubated at 37°C for 20 h. Cells were fixed after three washes and the permeabilization protocol was followed.

For costaining of the α-MUC1 ED and ACE2, fixed cells on coverslips were permeabilized in 70% absolute ethanol (Merck) for 10 min. After permeabilization, cells were washed two times with DPBS and then blocked with 0.6% BSA in DPBS for 30 min. Cells were incubated onto 75-µl drops containing 214D4 antibody (CD227, Nordic MUbio) diluted 1:100 for MUC1-ED and ACE2 antibody (AF933, R&D Systems) diluted 1:200 with 0.6% BSA in DPBS on parafilm overnight at 4°C. Afterwards three washing steps were performed. The coverslips were further incubated with the secondary antibodies Alexa Fluor 488-conjugated rabbit α-goat IgG (1:500; A11078, Invitrogen), Alexa Fluor 568-conjugated donkey α-mouse IgG (1:100; A10037, Thermo Fisher) and DAPI at 2 µg/ml (D21490, Invitrogen) for 1 h. Coverslips were washed 3 times with DPBS, washed a final time with MilliQ, dried, embedded in Prolong diamond mounting solution (Thermo Fisher), and allowed to solidify overnight at RT.

A Leica SPE-II confocal microscope (Leica Microsystems, Wetzlar, Germany) was used to acquire single plane images with a 40X objective (NA 1.3, HCX PLANAPO oil) controlled by Leica LAS AF software with default factory settings. A quad band dichroic was used, allowing diode laser wavelengths 405, 488, 561 nm lines to pass and fluorescent signal to enter the prism to sequentially detect DAPI, Alexa Fluor 488, Alexa Fluor 568/594, Alexa Fluor 647. Images stacks were collected using a 63X oil immersion objective in bidirectional mode (average 16). Sequential laser illumination through a quadband dichroic (405, 488, 561, and 647) was used in combination with emission factor default spectral detection of DAPI, Alexa Fluor 488, Alexa Fluor 568/594, and Alexa Fluor 647, respectively. XZ and YZ Orthogonal views of 30-pixel thickness are shown generated in either Imaris (Oxford Instruments version 8.2, Belfast, UK). Acquired images were processed in Leica Application Suite X (LAS X; Leica).

879 Maximum intensity projections are shown, as well as representative slices from the image series. Final
880 outlining of the figures was performed in Adobe Illustrator (Adobe Inc., San Jose, USA).
881 Fluorescent spike signal was quantified by ImageJ software (54). A segmented line (line width=10) was
882 outlined along the edge of the cell island to select the region of interest (ROI) in control, StcE and
883 E447D treated Calu-3 cells. The sum of all pixels in the ROI was measured by Raw Integrated Density
884 (RawIntDen) and the bar diagram was represented as RawIntDen/length (µm). Three random regions
885 were selected, and three independent experiments were performed.
886 Spinning disk imaging was performed on an Olympus SpinSR10 system equipped with a Yokogawa W1-
887 SoRa spinning disk mounted on a IX83 stand with an ORCA Flash 4.0 camera (Olympus, Leidendorp,
888 the Netherlands). The system was run in confocal mode using a 60 x Uplan Apo OHR objective (NA 1.5)
889 and multiband dichroic to sequentially illuminate 405, 488 and 561 nm laserlines, emission filter
890 wheels set to detect 447/60, 525/50 and 617/73 bandwidths for DAPI, Alexa488 and Alexa568
891 respectively. Images were deconvolved using maximum likelihood estimation in 5 iterations in
892 CellSense Dimension (Olympus) and intensity adjusted.